WL-TR-96-2125

FUNDAMENTAL STUDIES IN CRYOGENIC COOLING OF POWER ELECTRONICS

L. C. CHOW M. S. SEHMBEY
X. Q. CHEN

UNIVERSITY OF KENTUCKY
DEPARTMENT OF MECHANICAL ENGINEERING
LEXINGTON, KY 40506-0046

SEPTEMBER 1996

FINAL REPORT FOR 09/01/95-08/31/96

APPROVED FOR PUBLIC RELEASE; DISTRIBUTION IS UNLIMITED.

AEROPROPULSION AND POWER DIRECTORATE
WRIGHT LABORATORY
AIR FORCE MATERIEL COMMAND
WRIGHT PATTERSON AFB, OH 45433-7251

NOTICE

When Government drawings, specifications, or other data are used for any purpose other than in connection with a definitely Government-related procurement, the United States Government incurs no responsibility or any obligation whatsoever. The fact that the government may have formulated or in any way supplied the said drawings, specifications, or other data, is not to be regarded by implication, or otherwise in any manner construed, as licensing the holder, or any other person or corporation; or as conveying any rights or permission to manufacture, use, or sell any patented invention that may in any way be related thereto.

This report is releasable to the National Technical Information Service (NTIS). At NTIS, it will be available to the general public, including foreign nations.

This technical report has been reviewed and is approved for publication.

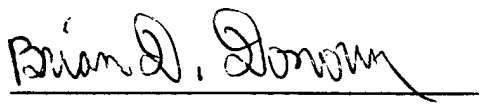

BRIAN D. DONOVAN
Mechanical Branch
Aerospace Power Division

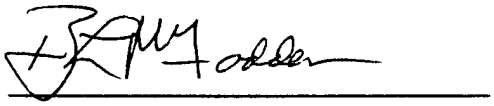

BURYL L. MCFADDEN
Chief, Mechanical Branch
Aerospace Power Division

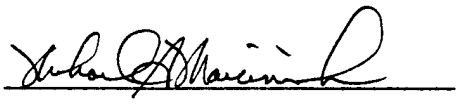

MICHAEL A. MARCINIAK, Major, USAF
Deputy Director
Aerospace Power Division

If your address has changed, if you wish to be removed from our mailing list, or if the addressee is no longer employed by your organization please notify WL/POOS , WPAFB, OH 45433-7251 to help us maintain a current mailing list.

Copies of this report should not be returned unless return is required by security considerations, contractual obligations, or notice on a specific document.

REPORT DOCUMENTATION PAGE

Form Approved
OMB No. 0704-0188

1. AGENCY USE ONLY *(Leave blank)*	2. REPORT DATE	3. REPORT TYPE AND DATES COVERED
	SEP 1996	FINAL 09/01/95-08/31/96

4. TITLE AND SUBTITLE
Fundamental Studies in Cryogenic Cooling of Power Electronics

5. FUNDING NUMBERS
C F33615-91-C-2152
PE 63218
PR 1601
TA 05
WU 03

6. AUTHOR(S)
L. C. Chow M. S. Sehmbey
X. Q. Chen

7. PERFORMING ORGANIZATION NAME(S) AND ADDRESS(ES)
University of Kentucky
Department of Mechanical Engineering
Lexington, KY 40506-0046

8. PERFORMING ORGANIZATION REPORT NUMBER

9. SPONSORING/MONITORING AGENCY NAME(S) AND ADDRESS(ES)
Aero Propulsion and Power Directorate
Wright Laboratory
Air Force Materiel Command
Wright Patterson AFB OH 45433-7251
POC: Brian Donovan, WL/POOS (937)255-6241

10. SPONSORING/MONITORING AGENCY REPORT NUMBER
WL-TR-96-2125

11. SUPPLEMENTARY NOTES

12a. DISTRIBUTION/AVAILABILITY STATEMENT
Approved for public release; distribution is unlimited

12b. DISTRIBUTION CODE

13. ABSTRACT *(Maximum 200 words)*

This report is divided into two studies. The first deals with the measurement and modeling of film thickness produced during spray cooling. The experiments were conducted using pressure and air atomizing nozzles. The film thickness increases with decrease in flow rate for pressure atomizing nozzles, although the decrease is small. For air atomizing nozzles, increase in flow rate causes an increase in film thickness while and increase in air velocity causes a decrease in film thickness. Models were derived for both forms of sprays. The second study deals with the effect of operating temperature and cooling technique on power MOSFET characteristics. This numerical study found that the maximum drain current can be more than quadrupled at 78 K as compared to room temperature operation. In comparing spray cooling and immersion cooling, it was found that the maximum drain current possible with spray cooling was more than double that with immersion cooling.

14. SUBJECT TERMS
Cryogens, Spray Cooling, Film Thickness, Immersion Cooling, Cryo-Electronics, Power MOSFETs, Low Temperature

15. NUMBER OF PAGES
53

16. PRICE CODE

17. SECURITY CLASSIFICATION OF REPORT	18. SECURITY CLASSIFICATION OF THIS PAGE	19. SECURITY CLASSIFICATION OF ABSTRACT	20. LIMITATION OF ABSTRACT
Unclassified	Unclassified	Unclassified	SAR

GENERAL INSTRUCTIONS FOR COMPLETING SF 298

The Report Documentation Page (RDP) is used in announcing and cataloging reports. It is important that this information be consistent with the rest of the report, particularly the cover and title page. Instructions for filling in each block of the form follow. It is important to ***stay within the lines*** to meet ***optical scanning requirements***.

Block 1. Agency Use Only *(Leave blank)*.

Block 2. Report Date. Full publication date including day, month, and year, if available (e.g. 1 Jan 88). Must cite at least the year.

Block 3. Type of Report and Dates Covered. State whether report is interim, final, etc. If applicable, enter inclusive report dates (e.g. 10 Jun 87 - 30 Jun 88).

Block 4. Title and Subtitle. A title is taken from the part of the report that provides the most meaningful and complete information. When a report is prepared in more than one volume, repeat the primary title, add volume number, and include subtitle for the specific volume. On classified documents enter the title classification in parentheses.

Block 5. Funding Numbers. To include contract and grant numbers; may include program element number(s), project number(s), task number(s), and work unit number(s). Use the following labels:

C	- Contract	PR	- Project
G	- Grant	TA	- Task
PE	- Program Element	WU	- Work Unit Accession No.

Block 6. Author(s). Name(s) of person(s) responsible for writing the report, performing the research, or credited with the content of the report. If editor or compiler, this should follow the name(s).

Block 7. Performing Organization Name(s) and Address(es). Self-explanatory.

Block 8. Performing Organization Report Number. Enter the unique alphanumeric report number(s) assigned by the organization performing the report.

Block 9. Sponsoring/Monitoring Agency Name(s) and Address(es). Self-explanatory.

Block 10. Sponsoring/Monitoring Agency Report Number. *(If known)*

Block 11. Supplementary Notes. Enter information not included elsewhere such as: Prepared in cooperation with...; Trans. of...; To be published in.... When a report is revised, include a statement whether the new report supersedes or supplements the older report.

Block 12a. Distribution/Availability Statement. Denotes public availability or limitations. Cite any availability to the public. Enter additional limitations or special markings in all capitals (e.g. NOFORN, REL, ITAR).

- **DOD** - See DoDD 5230.24, "Distribution Statements on Technical Documents."
- **DOE** - See authorities.
- **NASA** - See Handbook NHB 2200.2.
- **NTIS** - Leave blank.

Block 12b. Distribution Code.

- **DOD** - Leave blank.
- **DOE** - Enter DOE distribution categories from the Standard Distribution for Unclassified Scientific and Technical Reports.
- **NASA** - Leave blank.
- **NTIS** - Leave blank.

Block 13. Abstract. Include a brief *(Maximum 200 words)* factual summary of the most significant information contained in the report.

Block 14. Subject Terms. Keywords or phrases identifying major subjects in the report.

Block 15. Number of Pages. Enter the total number of pages.

Block 16. Price Code. Enter appropriate price code *(NTIS only)*.

Blocks 17. - 19. Security Classifications. Self-explanatory. Enter U.S. Security Classification in accordance with U.S. Security Regulations (i.e., UNCLASSIFIED). If form contains classified information, stamp classification on the top and bottom of the page.

Block 20. Limitation of Abstract. This block must be completed to assign a limitation to the abstract. Enter either UL (unlimited) or SAR (same as report). An entry in this block is necessary if the abstract is to be limited. If blank, the abstract is assumed to be unlimited.

TABLE OF CONTENTS

LIST OF ILLUSTRATIONS

NOMENCLATURE

D	orifice diameter of air atomizing nozzle, m
h	nozzle orifice to target surface distance, m
I_D	drain current, A
$\dot{m}$	local liquid flow rate, $kg/m^2 \cdot s$
M	total liquid flow rate, kg/s
P_D	power dissipation, W
p	pressure, Pa
p_0	stagnation point pressure, N/m^2
q''	heat flux, W/m^2
r	radial position, m
$R_{DS(on)}$	on-resistance of the MOSFET, Ω
R_{th}	thermal resistance, °C/W
Re_δ	Reynolds number, $Re_\delta = U_r \bullet \delta / \mu$
T	temperature, K or °C
u	liquid local velocity, m/s
U_r	liquid velocity at film free surface, m/s
V	average droplet velocity, m/s
V_{air}	air jet velocity, m/s
w	velocity in z direction, m/s

Greek Symbols

α	droplet attack angle, $\cos\alpha = h / (r^2+h^2)^{1/2}$
δ	film thickness, m
ρ	liquid density, kg/m^3
μ	dynamic viscosity, $N \cdot s/m^2$
τ_s	surface shear force at the liquid-air interface, N/m^2

Subscripts

a	air
c	case
crit	critical
j	junction
l	liquid
m	average
sat	saturation

1. INTRODUCTION

The future of superconducting and low temperature MOS (metal-oxide semiconductor) electronics holds a great deal of promise. In some cases, the reductions in device sizes and the increased efficiency for liquid nitrogen temperature (LNT) operation may outweigh the cost. The most immediate applications will be in situations where a cryogenic liquid is readily available. In that case, the cryogen can be used as the heat transfer fluid and the size and weight of the onboard electronics can be reduced by an order of magnitude. However, the successful application of cryogenic cooling to electronics requires that the appropriate heat transfer characteristics be known. This is the main objective of this study.

The primary thermal management techniques for low temperature operation are: spray cooling, pool boiling (immersion cooling), forced convection boiling (or flow boiling), and jet impingement cooling. This report which is the final annual report for the contract F33615-91-C-2152 focusses on spray cooling and thermal management issues in cooling of power MOSFETs.

Spray cooling was chosen because of its capability in removing large quantities of heat at very low liquid flow rates. Experiments have been conducted for various spray cooling conditions using liquid nitrogen. The results of the experiments, and semi-empirical correlations for the heat transfer coefficient and critical heat flux, have been presented in previous annual reports for the contract [1-4]. Recently, new models for the estimation of the liquid film thickness in spray cooling were developed. Estimation of the film thickness is an important aspect of spray cooling analysis. The models for predicting film thickness produced by pressure atomizing nozzles and air atomizing nozzles are presented in this report.

The general issues concerning thermal management of cryo-electronics are also discussed in this report. The advantages of operating power MOSFETs at low temperatures are demonstrated through a numerical study. In addition, a comparison of the impact of different cooling techniques on MOSFET performance is presented.

2. OBJECTIVES

The overall objective of this study is to obtain information on the heat transfer characteristics under conditions of cryogenic cooling in various modes. Also, the suitability of these heat transfer modes to aerospace applications has to be evaluated. Due to the lack of suitable design correlations/models, experimental studies have to be undertaken to evaluate the heat transfer characteristics of liquid nitrogen under: pool boiling in complex geometries, spray cooling, forced convection boiling, and jet impingement. This would be followed by the development of design correlations for these modes of cooling. Finally, the applicability of these techniques to electronic cooling has to be demonstrated.

3. BACKGROUND

The electronic systems envisaged for operation at LNT fall into two categories. First, the superconducting circuits composed of high temperature superconducting (HTS) devices (switches, capacitors, inductors, etc.), and second, the hybrid circuits which contain both HTS and semiconductor devices. There are numerous applications for both types of circuits. These two configurations and their applications are discussed in the following sections.

3.1 Superconducting Circuits

Superconducting circuits will consist of HTS devices (logic gates, inverters, memory cells, etc.) with superconducting interconnects [5]. Almost all of the functions performed in high performance electronics can be done by a superconductor circuit [6]. However, superconductor circuits cannot handle high power levels; also, there are no superconducting rectifiers, and semiconductors make better amplifiers and mass memory devices. The main applications of HTS circuits will be

- High speed digital logic and memory: gate speeds under 10 ps are easily achievable using Josephson junctions [5,6] thus allowing the development of faster supercomputers;
- Far infrared/high frequency radar detection: with circuits employing Josephson junction device mixers, very-low-noise high-frequency detection (over 100 GHz) is possible with the only limitation being the Heisenberg uncertainty principle [5,7,8];
- Magnetic field sensors: very sensitive magnetometers and voltmeters made using SQUIDs (superconducting quantum interference devices) have application in magnetic field geophysical exploration and biomagnetic studies of the human body; and
- Superconducting-coil magnets and motors: superconducting-brushless-ac motors can be used in various applications.

3.2 Superconductor/Semiconductor Hybrid Circuits

MOS semiconductor devices show a marked improvement in performance as the operating temperature is lowered [6,9,10]. Furthermore, the thermal conductivities of semiconductor substrates and packaging materials (silicon, germanium, beryllium, alumina) are seen to increase dramatically as the temperature is lowered to LNT [11]. The main advantages of low temperature operation are: increased electron and hole mobilities, lowered interconnection resistivities, reduced leakage currents, greater subthreshold slope, and reduction in thermal noise. One of the possible applications of low temperature electronics will be in the area of high efficiency ac/dc, dc/ac and RF power conversion at the multikilowatt level. As mentioned earlier, superconducting circuits are not capable of handling high power levels. Hence, MOS field effect transistors (MOSFETs) can be used in combination with high Q inductors and capacitors made from HTSs to obtain the zero voltage switching circuits suitable for power conversion applications [10]. Such an integration will result in a drastic size and weight reduction. The efficiency of these circuits improves greatly at low temperatures due to the dramatic reduction in the on-resistance of power MOSFETs. However, the efficiency of these circuits depends greatly on the Q values of the inductors and capacitors used in the circuit. Hence, it is necessary to use HTSs for these components to obtain the maximum efficiency. Another application of hybrid circuits is the high-frequency receiver-signal processor [6]. Here, the devices best suited for each component of the circuit are used. Thus, a combination of superconductor and semiconductor devices provides a high performance circuit. In industry and transportation, the HTS ac motors employing MOSFET controllers have variety of applications. The HTS-ac motors have been successfully tested recently and will be commercially available in the near future [12]. At the same time, locomotive engines using natural gas (stored at 110 K in liquid form) have been developed [13]. These two can be combined, with the liquefied natural gas acting as the coolant for the HTS motor and MOSFET switches, to produce a highly efficient and clean locomotive engine.

3.3 Thermal Management Issues

A cursory examination of heat transfer requirements in superconducting circuits may lead one to believe that due to the very nature of superconductivity heat dissipation would not be a

problem. However, a closer examination reveals how ill-founded that notion is. The main components in a superconducting circuit are the high-speed low-power switches, the Josephson junctions (also called Superconductor-Insulator-Superconductor devices, SISs) [6,8]. The main advantages of these devices are the low gate delay times and low power dissipation; these features in combination will allow much higher device packing density compared to semiconductor circuits. However, the thermal management aspect of superconducting circuits at LNT has been of concern lately. A typical SIS working at 4.2 K has a power dissipation of 50 kW/m^2, however, for operation at 77 K, the same device may have a heat dissipation approaching 6000 kW/m^2 [14]. Obviously, this level of heat dissipation cannot be handled by common heat removal techniques. Hence, there are two options available for the thermal management of HTS circuits:

1. Immersion cooling (pool boiling) in liquid nitrogen (LN_2) with low device density packaging employing heat spreaders; and
2. High heat flux cooling with LN_2.

The first option cannot be expected to handle device heat dissipation above 500 kW/m^2. This is because the pool boiling critical heat flux for LN_2 is only about 160 kW/m^2 (calculated using Zuber model [15]). Hence, even with good heat spreaders, the overall device dissipation could not be expected to be more than 2-3 times this amount. Thus, immersion cooling will mean larger, and thereby slower, devices. This may not be a concern in some applications. However, for high speed digital applications, device sizes have to be kept as small as possible in order to minimize the distance travelled by the signal. In those cases the second option of using a high heat flux cooling technique would be much more preferable.

A superconductor/semiconductor hybrid circuits is inherently more prone to thermal failure due to the presence of high heat dissipation transistors in the vicinity of superconducting elements. It is not possible to thermally isolate the superconductor and semiconductor elements because the interconnections themselves serve as thermal bridges. The successful operation of a hybrid circuits depends on the ability of the cooling system to maintain the superconducting elements below their transition temperature. Hence, it is essential that the cooling system is capable of removing high heat fluxes from discrete locations (MOSFETs) to prevent any hot spots and the resultant system failure. Again, in this case, the choices are similar to the ones mentioned before.

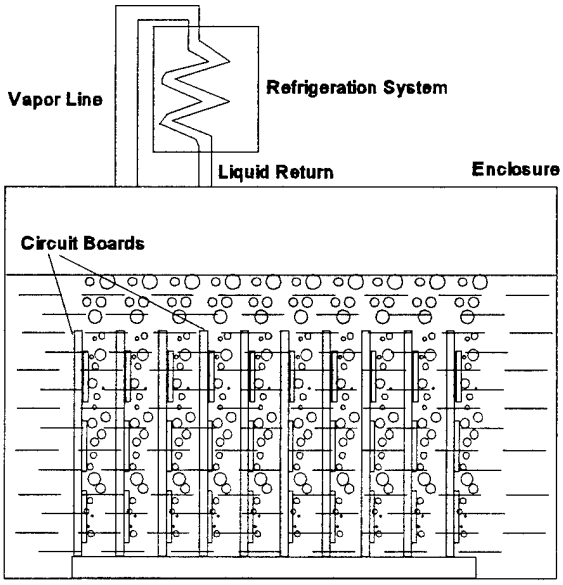

Immersion (Pool Boiling) Cooling

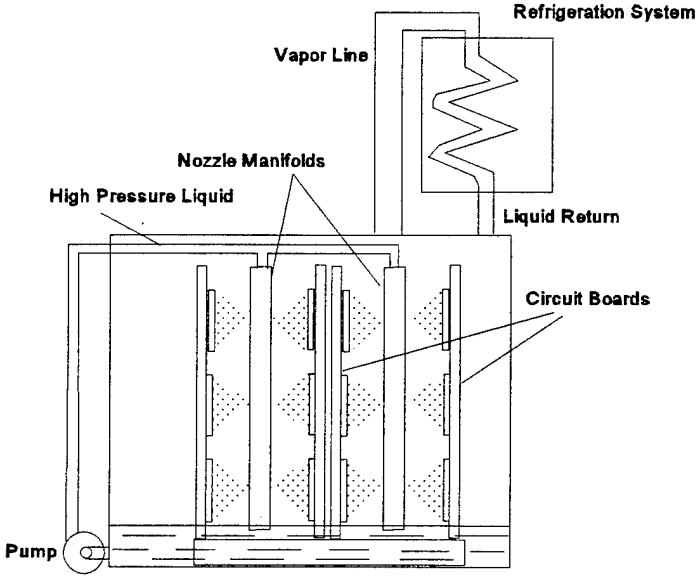

Spray Cooling System

Figure 3.1 Low Temperature Cooling Scenarios.

Thus, the thermal management scenario in low temperature electronics consists of either using direct immersion pool boiling with heat spreaders, or, a high heat flux cooling technique. For the high heat flux situation, spray cooling is the technique which is of most interest because of its low liquid flow rate requirements. Low temperature spray cooling consists of subjecting the heat sources with a high speed spray of low temperature liquid. The two thermal management scenarios described above are shown in Figure 3.1. As shown in the figure, both scenarios require a refrigerator/condenser unless the low temperature liquid is available in abundance (as in the case of stored liquefied fuel). The spray cooling scenario will also require a pump for cases where a high pressure liquid is unavailable.

The main concern regarding these techniques is the lack of information about the heat transfer characteristics of cryogens under the particular conditions described above. Liquid nitrogen was selected as the cryogen for the heat transfer studies due to its suitability for both HTS and MOS devices. The heat transfer characteristics of spray cooling with liquid nitrogen were not available. Also, no general correlations were available for spray cooling. Thus, the spray cooling part of this study dealt with determining the heat transfer characteristics and obtaining suitable correlations. As mentioned earlier, the experimental data and correlations have already been presented in previous reports [1-4]. In Section 4 of this report, new models are presented for estimating the liquid film thickness, and important aspect of spray cooling analysis. In case of pool boiling, the previously available correlations dealt with simple situations only (e.g., single heater in an unconfined pool of liquid nitrogen). However, the conditions in electronic cooling are far more complex due to the interaction of various heaters and lack of space. Thus, the pool boiling part of this study dealt with the effects of multiple heat sources and confined space. The results of that investigation and the resulting predictive correlations were presented in the previous resports [3,4]. In Section 5, the influence of operating temperature on the drain current and power dissipation characteristics of power MOSFETs is examined using numerical analysis. In addition, the influence of two different cooling techniques, immersion cooling and spray cooling, is also examined.

4. FILM THICKNESS IN SPRAY COOLING

Spray cooling is the method of using small-size, high-velocity droplets impinging on a heated surface to remove the heat (Figure 4.1). Spray cooling can be divided into two categories based on the method of spray generation. A pressure atomizing nozzle can be used to atomize the liquid using the pressure difference across the nozzle, or, a high-velocity gas stream can be used to break up a liquid jet into a spray. In recent years significant research has been conducted on the heat transfer characteristics of spray cooling [16 - 19]. It has been shown that spray cooling can achieve high critical heat fluxes ($>10^7$ W/m^2 with water on a 1 cm heater) and high heat transfer coefficients (can be as high as $3x10^5$ w/m^2°C with water)[17 -19]. Compared with jet impingement, spray cooling requires less amount of liquid to achieve similar heat transfer coefficient [20].

4.1 Objectives of this Study

Up to the present, relatively little is known about the heat transfer process in spray cooling. Among the important mechanisms involved in spray cooling, film flow on the heated surface is one of the most important ones. Better understanding of the film flow in spray cooling will help in estimating the convective heat transfer, incipience of boiling in the film, the phase change heat transfer and the CHF (critical heat flux).

Because of the different atomizing methods used and the different flow fields near the heated surface, the film flows produced by sprays generated by air atomizing nozzles and pressure atomizing nozzles are different. In the present work, the film thickness produced by pressure atomizing nozzles and air atomizing nozzles are studied experimentally and theoretically. The point gauge method is used to measure the film thickness and numerical and analytical methods are used in the modeling of the film flow. Since liquid nitrogen is a dielectric liquid, it is not possible to employ this method of film thickness measurement for liquid nitrogen sprays. Hence, this study is conducted with water, but the results can be extended to any liquid.

4.2 Literature Review

Yang et al. [21] measured the film thickness of an air atomizing nozzle using the Fresnel diffraction method. The advantage of this method is that it is a non-invasive method. The film

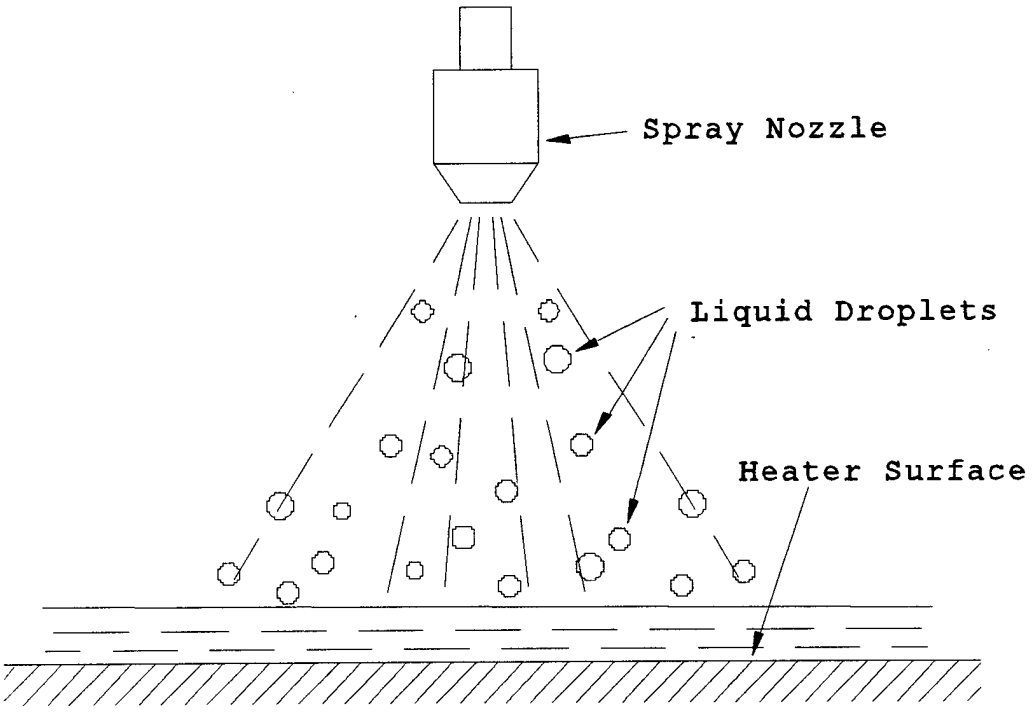

Figure 4.1 Spray Cooling

thickness was measured by the change in the line of sight using a laser beam. Time average was used in the final measured film thickness. The experiments were carried out on a 10×10 mm glass surface with an air atomizing nozzle situated 11 mm above. They showed that with a fixed air pressure, the film thickness is very sensitive to the liquid flow rate, the film thickness changes from 85±15 μm at 1 liter/hr to 235±75 μm at 4 liters/h when the air pressure is at 138 kPa (20 psig). Unfortunately no results were shown for the film thickness at air pressures other than 138 kPa. The air velocity which depends on the air inlet pressure could be one of the dominant factors that affects the film thickness of the air atomizing nozzles. In the same paper, Yang et al. also measured the topography of the water film using a holographic technique. In their experiment, a laser beam was split into two beams and one of them was made to pass through the liquid film. Focusing these two beams together results in an interference pattern. By recording and measuring the distance between the fringes, the topography of the film can be obtained. Results showed that the overall *change in flatness is only about 1 μm*, which is negligible *compared with the measured film thickness*. Therefore, the authors concluded that the liquid film produced by air atomizing nozzles is flat.

Yang et al. [22] used an analytical model to analyze the film thickness produced by air

atomizing nozzles. They assumed a laminar film flow and used the stagnation flow pressure gradient of the air flow field in their model. The liquid film thickness prediction agrees well with their experimental data.

Siwon [23] also measured the film thickness produced by an air atomizing nozzle. The method used was a flush-mounted conductive probe. The author measured the thickness of the entire film from the stagnation point to the point where the hydraulic jump occurs. The results indicate that the film thickness was usually less than 10^{-4} m. Reaching the lowest value at the impinging point, the film thickness grows visibly in the stagnation area but thereafter remains constant up to the hydraulic jump. The experiments were conducted with different liquids and air flow rates as well as different nozzle heights. Unfortunately the author did not provide the geometry of the nozzles and no information can be obtained for the air speed, which makes the comparison of the results very difficult. The author also compared the film thickness of water jet and spray for approximately the same water flow rate. The results show the film thickness produced by air atomizing nozzles is up to one order of magnitude lower than that of a liquid jet.

Tilton [18] measured the film thickness produced by pressure atomizing nozzles. He measured the film thickness after the hydraulic jump and calculated the film thickness before the jump using the hydraulic jump theory. The results indicate that the film thickness varies from 130 μm to 340 μm for the five nozzles used, with the liquid flow rate varying from 4.5 to 7.5 cc/s. The film thickness does not change significantly with the different nozzle orifices, especially at the lower liquid flow rates. However this method may not be accurate in predicting the film thickness in the spray core because the hydraulic jump occurs some distance away from the spray core and the film thickness may change within that distance.

4.3 Experiment Description

4.3.1 Point Gauge Method

Needle probes have been used to measure the film thickness in the past [18,24]. This method uses a needle probe, a conductive surface and a precise micrometer to measure the distance between the probe and the conductive surface (Figure 4.2). The film thickness is determined by measuring the electrical resistivity between the needle probe and the conductive surface. The advantage of this

method is that it is simple and direct. When the liquid surface is stable, the accuracy mainly depends on the micrometer, which can be very precise. One of the concerns in using this method to measure the film thickness in the spray core is that since the entire surface is being bombarded by the droplets, the presence of the needle probe may interfere with the integrity of the flow field. But, since the liquid is flowing outward in the radial direction in the spray core, the probe only interferes with the flow in the region behind it. By selecting the smallest possible probe diameter and setting the probe along the radial direction with an angle to the surface the interference of the probe for the area ahead of it can be reduced.

Previous measurements of the film thickness have been based on the sudden and significant change in resistance as the probe leaves or touches the liquid surface. Unfortunately, when measuring the film thickness produced by a pressure atomizing nozzle, this sudden change in resistance does not occur in the spray core. Figure 4.3 shows a typical signal when the probe tip is

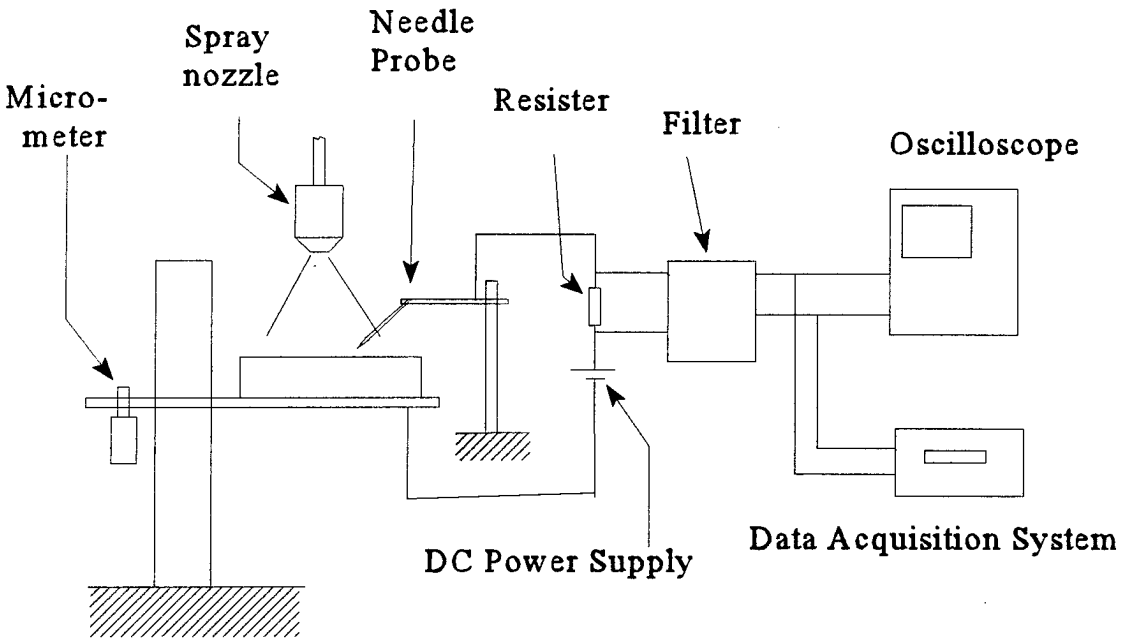

Figure 4.2 Experimental Set-up

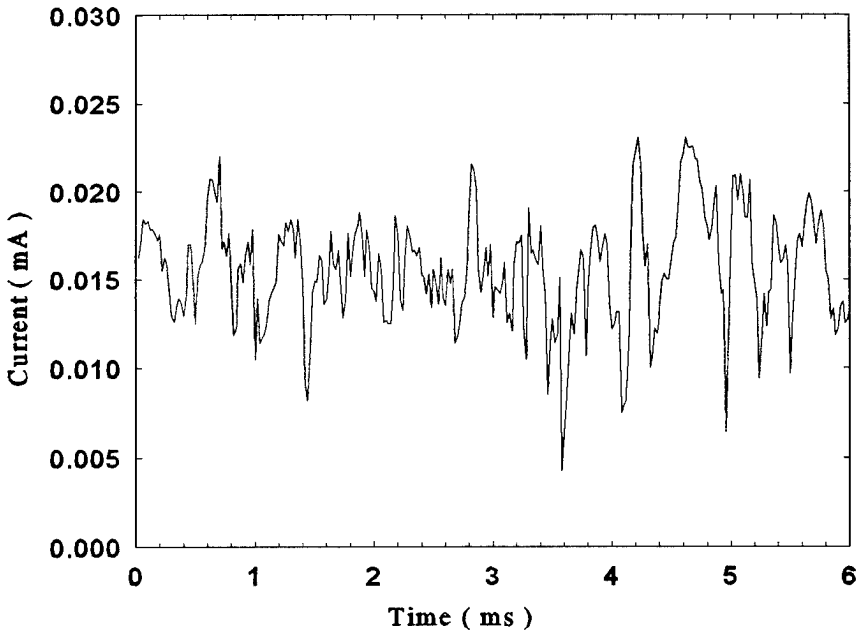

Figure 4.3 Typical Signal

near the film surface. The y axis is the current in the circuit that reflects the resistance of water between the needle tip and the surface. This signal form maintains the same characteristics and no abrupt resistance change can be observed as the probe moves up and down in the spray core. The reason is that the film in the spray core has a wavy surface that yields oscillating signals near the surface. Also, since the needle is constantly hit by the droplets in the spray core, even when the tip is already above the liquid surface there will still be liquid dripping down at the needle tip which provides a conductive path (see Fig. 4.4). Instead of a conspicuous resistance change at the liquid surface, this dripping liquid makes the resistance change gradually with the distance between the needle tip and the surface. However, the rate of resistance change will be different when the needle tip is at different positions (in the film, near the wavy film surface and above the film surface) due to the different conductive paths. The difference of resistance change rates is more repeatable when the time average of the signal is used. Figure 4.5 is a typical current-distance curve measured in the experiments using a pressure atomizing nozzle. The X-axis is the distance between the needle tip

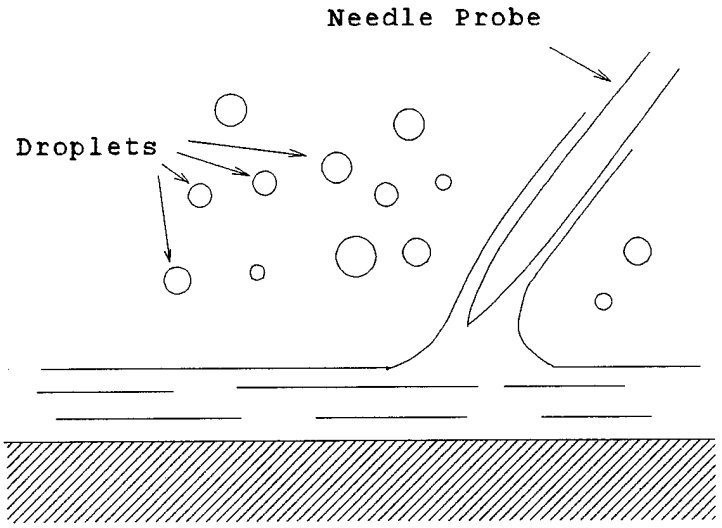

Figure 4.4 Conductive Path at the Needle Tip

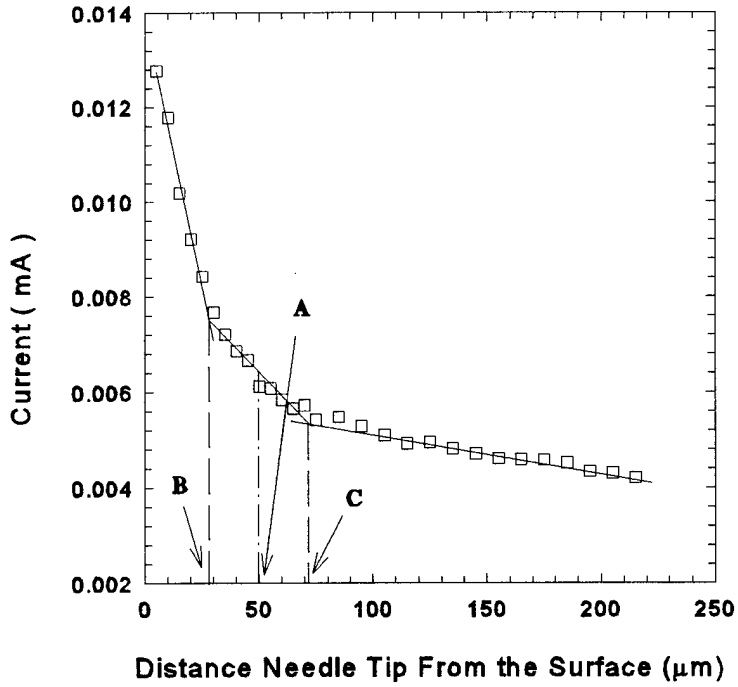

Figure 4.5 Method of Locating Film Surface

and the surface. The Y-axis is the current in the circuit shown in Figure 4.2. Time average is used for the current. At both ends of the curves there are always two linear sections with different slopes. These are the sections when the needle tip is in and out of the film. The middle point of the mid section (point A in Fig. 4.5) gives the average position of the film surface.

The signals are much simpler for the air atomizing nozzle. The high velocity air blows away the dripping liquid at the needle tip and at the same time the film surface is more stable and flat as compared to the pressure atomizing nozzle because of the finer droplets and the favorable pressure gradient and the surface shear force caused by the air flow. In this case, the signal when the needle tip touches the film surface is as clear and strong as when measuring a stable film without the presences of droplets or air flow.

4.3.2 Electrolysis Property of Water

The voltage corresponding to the Gibbs free energy of water at room temperature is about 1.22 V [25]. Water molecules will dissociate if the voltage across the two electrodes is larger than this voltage. Preliminary measurements showed that if the voltage drop on the water is less than 1.22 V, the signal is too weak and the relation between the resistance and the distance between the electrodes cannot be used reliably to measure the film thickness. If the voltage on the water film is higher than 1.22 V, ions begin to be generated and the resistance changes significantly with the distance between electrodes in the flowing water film. This is the property needed in the film thickness measurement.

The resistance also changes with the velocity of water for a fixed inter-electrode distance when using a high voltage. This is because more ions will be washed away when the water velocity is higher. This makes the resistance increase with water velocity when the ions form the main conductive medium. This phenomenon prevented us from using the calibrated resistance-distance table to measure the film thickness. However it is not a problem if we use the method described earlier to find the film thickness.

4.3.3 Experiment Set-up and Procedure

The schematic diagram of the experiment set-up is presented in Figure 4.2. The surface on which film thickness is measured is the polished flat end of a stainless steel cylinder with a diameter

of 62 mm. The surface has a mirror finish which reduces the effect of surface roughness on the film flow. The cylinder sits on an adjustable platform to keep it horizontal. This platform is attached firmly to a micrometer which has a resolution of 2 μm. The probe is made of a stainless steel needle covered with dielectric paint. Only the tip of the needle is exposed. The needle is attached to a firm stand and is set at an angle of 45° with respect to the horizontal surface. Before each experiment, the surface is cleaned and adjusted to ensure it is in a horizontal position.

When measuring the film thickness produced by pressure atomizing nozzles, *for each test run,* the cylinder is first moved upwards until the needle tip touches the solid surface. This point is set to zero. Then the surface is moved down in 5-μm increments. The increments are increased to 10 μm when the needle tip is 75 μm away from the surface. The time-averaged voltage on the resistor is recorded at every step. The current versus distance between the needle tip and the surface is then plotted. The method described earlier (Figure 4.5) is then used to determine the film thickness. Because of the reasons discussed in Section 4.3.2, a stabilized 5 V DC power supply and a 120 K resistor are used to form the circuit. The actual voltage drop on water is around 3.2 ~ 5 V. The voltage output on the resistor is connected to an adjustable low-pass filter. The filtered signals are measured by the data acquisition system and monitored by an oscilloscope at the same time. Because the film has a wavy surface and the resistance changes with the velocity, the current in the circuit oscillates violently when the needle tip is near the film surface (see Fig. 4.3). The data acquisition system with a maximum data acquisition speed of 50 kHz cannot provide enough resolution for the signal. Hence, a low-pass filter is used to eliminate the high frequencies in the signal and the data acquisition system is then used to measure the time average of the voltage output.

The surface tension does not affect the film thickness measurement in this case because the liquid film is flowing. This is proven by the identical results when the film thickness is measured by moving the surface upwards (reversed direction compared with the way described above).

An adjustable speed gear pump is used to pump the liquid at a stable flow rate and liquid pressure. The liquid flow rate is measured with a calibrated orifice meter and pressure transducer combination.

For the air atomizing nozzle, the same procedure is followed to get the zero point at which the needle tip touches the metal surface. Then the cylinder is moved down until the signal shows the contact between the needle tip and the liquid surface is missing. Since the film surface is still wavy,

an average is taken between the film thickness when needle tip begins to leave the surface and the thickness when the needle tip completely leaves the film. Usually this difference was less than 10 μm. Because of the high speed air flow, the surface tension also has little effect on the film thickness results even though the liquid speed is lower in this case. This is also proven by the identical results when the film thickness is measured by moving the surface upwards (reversed direction compared with the way described above). The measurement procedures described in this section are carried out for different combinations of nozzles, liquid flow rates and air pressures (for air atomizing nozzle).

The droplet speed is measured using a Phase Doppler Particle Analyzer (PDPA). The PDPA system is also used to measure the liquid flow rate distribution of the air atomizing nozzle. The mass flow rate distribution in the spray core of the pressure atomizing nozzle is measured by a small orifice collector, because the PDPA system cannot give reliable results for high droplet density sprays containing large droplets. The air speed of the air atomizing nozzle is measured by a pitot tube. City water at room temperature is used in all the experiments.

4.4 Results and Discussion

4.4.1 Results for the Pressure Atomizing Nozzle

Two nozzles, TG4 and TG6 (from Spray Systems, Inc.), with orifice diameters 0.559 mm and 0.686 mm respectively, were used in the experiments. The spray characteristics are listed in Table 4.1. The velocity is generally uniform across the spray core. So only the mean velocity is listed in Table 4.1. The mass flow rate distribution varies dramatically between the two nozzles. Figure 4.6 shows the mass flow rate distributions of TG4 and TG6 along one radial direction at 276 kPa (40 psig). Since only the distribution is of concern, the Y-axis is plotted in a relative scale. As the measurements show, the shapes of distribution curves are similar. The liquid flow rate is low near the center of the core and most of the liquid flow is concentrated near the edge.

Table 4.1 Droplet Velocity Measurement Results

Nozzle Inlet Pressure (kPa)		207	276	345	414
TG4	Mean Droplet Velocity (m/s)	16.5	18.8	21.2	23.4
	Liquid Flow Rate (cc/s)	4.9	5.3	5.7	6.1
TG6	Mean Droplet Velocity (m/s)	14.5	16.6	18.6	19.9
	Liquid Flow Rate (cc/s)	5.9	6.5	7.4	8.0

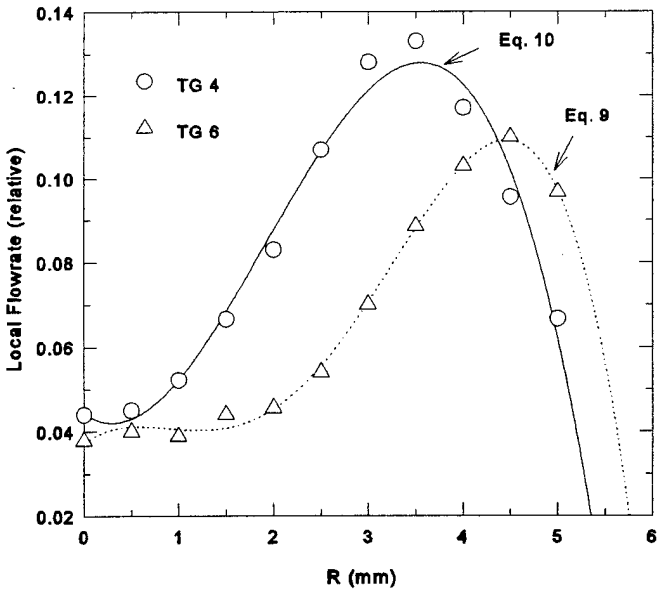

Figure 4.6 Flow Rate Distribution, Pressure Atomizing Nozzles

The results of the film thickness measurements are shown in Table 4.2. Two nozzle heights were used to determine the effect on the film thickness. The measurements are made near the outer edge of the spray core (R = 3 mm when the nozzle is 10 mm high and R = 5 mm when the nozzle is 15 mm high). The results show that for the liquid flow rates tested, there is only a slight decrease of the film thickness with the increase of liquid flow rate (or nozzle operating pressure). Different nozzle heights (10 mm and 15 mm) did not appear to affect the film thickness very significantly, although a slight increase in film thickness is seen with increase in nozzle height for most cases. For the two kinds of nozzles used in the experiments (TG4 and TG6), the results show no obvious relation between the film thickness and the nozzle orifice diameter. The film thickness remains at about 50 μm in most of the experiments. Radial film thickness profile measurement was also performed. Table 3.3 lists one set of results for these measurements. Within the accuracy that the present method can provide, no obvious film thickness change was observed across the spray core.

Table 4.2 Film Thickness Measurement Results

Pressure (kPa)			207	276	345	414
Film Thickness (μm)	10 mm Nozzle Height	TG4	54	47	44	43
		TG6	50	50	47	42
	15 mm Nozzle Height	TG4	62	46	46	46
		TG6	60	54	54	52

Table 4.3 Cross Section Film Thickness
(TG4, 276 kPa, 15-mm Nozzle Height)

R	0	2 mm	3.5 mm	5 mm
Film Thickness(μm)	54	45	44	46

4.4.2 Results for the Air Atomizing Nozzle

The air atomizing nozzle used in the experiment is one of the air brushes made by Paasche Airbrush Company. The nozzle geometry is shown in Figure 4.7. The nozzle is placed 20 mm above the surface and is connected to a gear pump and a compressed air source.

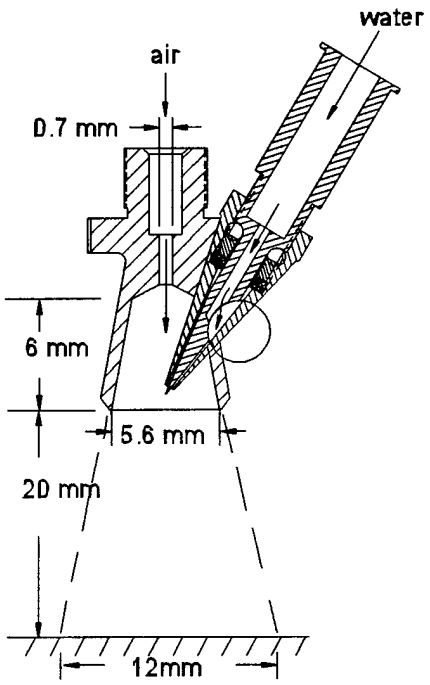

Figure 4.7 Air Atomizing Nozzle

Using a PDPA system to measure mass flux has some limitations, especially for high droplet density flows which involve large droplets. But, for the air atomizing nozzle used in this experiment, and the liquid flow rates tested, the PDPA system proved to be able to give reliable volume flux results. So the PDPA system is used to measure the liquid flow rate distribution of the air atomizing nozzle in this study. The mass flux is measured in 0.5 mm intervals across the spray core with a distance of 20 mm from the nozzle orifice (without any surface blocking the spray). This distance is also the distance where the surface is placed for film thickness measurements. Figure 4.8 shows one set of results. Contrary to the pressure atomizing nozzle, the maximum mass flux occurs near the center of the spray core and it decreases towards the edge of the spray core. Measurements also show the mass flux profile is not always symmetric because of the asymmetric design of the nozzle (see Figure 4.7).

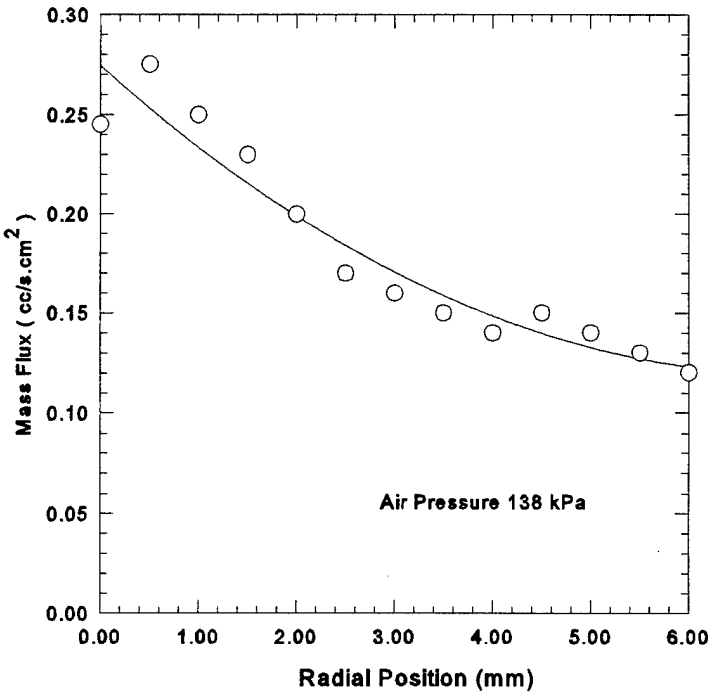

Figure 4.8 Mass Flux Distribution for the Air Atomizing Nozzle

The air velocity profile was measured with a pitot tube 20 mm from the nozzle orifice (Figure 4.9). The measurements were carried out at intervals of 0.5 mm. The air velocity profile shows the typical profile of a fully developed jet. But compared with the nozzle diameter (0.7 mm), the jet diameter (~10 mm) at 20 mm away from the orifice is extraordinarily large compared with that of ordinary jet nozzles. This high expansion rate is caused by the unique conical nozzle design (Figure 4.7) which makes the air jet different from the jet of an ordinary nozzle. We will consider this difference in the analysis.

The film thickness produced by an air atomizing nozzle is measured using the same set-up described earlier. The nozzle is set vertically and is 20 mm from the surface. At this distance, most of the droplets hit in a circle with a diameter of around 12 mm. The combinations of three air pressures (138 kPa, 207 kPa and 276 kPa) and five liquid flow rates (1.2, 1.8, 2.4, 3.0, 3.6 and 4.2 liters/hr) were tested. The results are listed in Table 4.4. As shown in the table, the film thickness decreases with increase in air pressure for the same liquid flow rate. This also means that a higher

air velocity results in a thinner liquid film. The liquid flow rate also affects the film thickness. For the same air pressure, the film thickness increases with increase in the liquid flow rate.

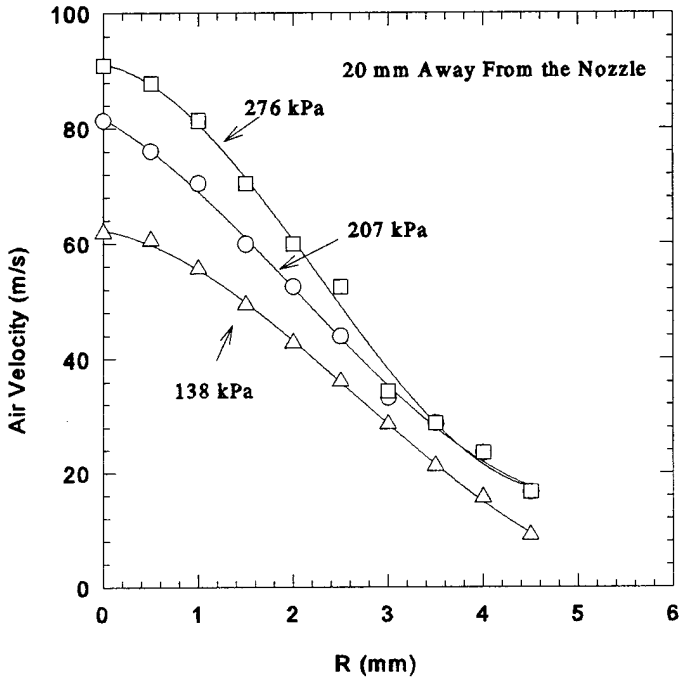

Figure 4.9 Air Velocity Profile for the Air Atomizing Nozzle

Table 4.4 Film Thickness Results, Air Atomizing Nozzle,
Nozzle Height 20mm, Orifice Diameter 0.7 mm

Liquid Volume Flow Rate [liter/hr]		1.2	1.8	2.4	3.0	3.6	4.2
Measured Film Thickness (μm)	Air Pressure 138 kPa	50	60	65	75	78	80
	207 kPa	35	40	42	45	47	50
	276 kPa	22	30	30	35	42	45

The film thickness at different locations in the spray core was also measured. Within the resolution of this method, no obvious change of film thickness in the spray core was observed. This result agrees with Yang's measurement [19,21] where he measured the topography of the film using the holography method with the same kind of nozzle. His measurements showed the flatness of the film is within 1 μm in the spray core.

4.5 Hydraulic Modeling of Film Flow

4.5.1 Pressure Atomizing Nozzle, Low Reynolds Number Flow

Low Reynolds number flow ($Re_\delta < 1510$) has been proven to have a strong damping factor and it can remain laminar under strong disturbance [26]. Even under unfavorable pressure gradient, low Reynolds number flow can still be stable [26].

For the nozzles and the flow rate range tested in the present study, the maximum Reynolds number based on the film thickness is about $Re_\delta = 580$ (TG6, 482 kPa) when the linear velocity profile is assumed. This is far below the critical Reynolds number $Re_{crit,\delta} = 1510$ [26]. So, despite the strong disturbance caused by droplet impingement, it is very likely that the film flow in the spray core is still laminar.

4.5.1.1 Hydraulic Modeling of the Film Flow

When the droplets hit the surface, the vertical component of the velocity is converted to pressure. Because of the dense spray (about 60,000 droplets/mm^2·s with a TG6 nozzle, liquid pressure: 275 kPa and nozzle height : 15 mm) and the high frequency of droplets impingement (60 kHz/mm^2 for the same case), the transient process of single droplet impingement will not be significant in the low Reynolds number film with a strong damping factor. So, we assume that the average pressure can be used in the analysis:

$$p = \bar{p} = \dot{m} V \cos\alpha = \frac{\dot{m} V h}{\sqrt{r^2 + h^2}} \qquad (4.1)$$

The pressure gradient caused by the impingement angle and mass flow rate distribution is:

$$\frac{dp}{dr} = \frac{-\dot{m}Vhr}{\sqrt{(r^2+h^2)^3}} + \frac{hV}{\sqrt{r^2+h^2}} \cdot \frac{d\dot{m}}{dr} \tag{4.2}$$

Figure 4.10 illustrates the pressure and shear force on the control volume and the mass flow across the boundary. The momentum change of liquid across the control volume is:

$$\frac{d}{dr}[\rho 2\pi r \int_0^{\delta} u^2 dy] \cdot dr - \dot{m} 2\pi r\, dr\, V \sin\alpha \tag{4.3}$$

The net force on the control volume is:

$$2\pi[-\frac{d}{dr}(r\delta p) - \tau_0 r]dr \tag{4.4}$$

where τ_0 is the surface shear force when y = 0:

$$\tau_0 = \mu \left.\frac{du}{dy}\right|_{y=0} \tag{4.5}$$

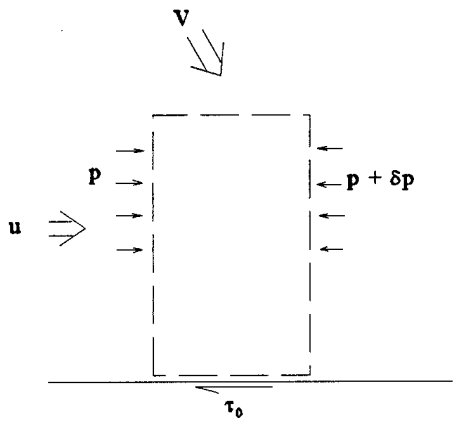

Figure 4.10 Control Volume for Momentum Equation

So the momentum equation for the control volume is:

$$-\frac{d}{dr}(r\delta p) - \tau_0 r = \rho\frac{d}{dr}(r\int_0^{\delta} u^2 dy) - \dot{m} r V \sin\alpha \tag{4.6}$$

The continuity equation can be obtained on a disc with a radius of r :

$$\dot{m}\pi r^2 = \rho 2\pi r \int_0^{\delta} u\, dy \tag{4.7}$$

For the laminar integral method, the results are usually not sensitive to the velocity profile. So we only use a third order polynomial for the velocity profile :

$$\frac{u}{U_r} = 3\eta - 3\eta^2 + \eta^3 , \qquad \eta = \frac{y}{\delta} \tag{4.8}$$

The mass flow rate profiles of TG6 and TG4 obtained from the experiments are as follow:

$$\dot{m} = M\cdot(0.037 - 17.23r + 2.38\times10^4 r^2 - 1.132\times10^6 r^3 - 1.355\times10^9 r^4)$$
$$TG6,\ h = 15mm,\ r = 0\sim5.5mm \tag{4.9}$$

$$\dot{m} = M\cdot(0.044 - 16.03r + 2.883\times10^4 r^2 - 4.983\times10^6 r^3)$$
$$TG4,\ h = 15mm,\ r = 0\sim5mm \tag{4.10}$$

The mass flow rate distribution will affect the pressure profile [Equation (4.1)], and thus affect the film flow. But getting a unique equation for the mass flow rate profile is impossible. Reference 12 provides a more detailed discussion on radial and circumferential liquid distribution in the spray core. Ortman and Lefebvre [28] examined the spray characteristics of several nozzles of different design. They found that the circumferential mal-distributions can be seen in most of the nozzles. For the TG4 and TG6 nozzles used in the experiment, the radial mass flow rate distribution

is different and the circumferential mal-distributions were also observed. Therefore, in order to get better comparison between different nozzles, the mass flow rate profile of Equation 4.10 is used in most of the film thickness calculations, except when specified otherwise. Different mass flow distributions were also used in order to see their effect on the film thickness.

The effect of nozzle height is very important for applications. Nozzle heights of 10 mm and 15 mm were used for comparison with the experimental results.

When the velocity and the mass flow rate profile are substituted into Equations 4.2, 4.6 and 4.7, we can get a differential equation of the form :

$$f_1\,(\dot{m}, V, h, r, \rho, \mu)\,\frac{d\delta}{dr} = f_2\,(\delta, \dot{m}, V, h, r, \rho, \mu) \qquad (4.11)$$

Runge-Kutta method of the sixth order is used to integrate Equation 4.11. This equation is unstable for a small radius. Therefore, the integration is carried out from about r = 2 mm for 15 mm nozzle height and at 1.5 mm for 10 mm nozzle height. The factory specification of the spray angle of TG4 and TG6 is 54° - 63° depending on the nozzle inlet pressure. However, the mass flow rate profile measurements show that most of the mass flow is concentrated within 40° (see Figure 4.6), so the integrations are also done within that angle. Water properties at room temperature and the droplet velocities listed in Table 4.1 are used in the analysis.

4.5.1.3 Results and Discussion

Figures 4.11 to 4.16 present some of the numerical results. Figures 4.11 and 4.12 show the film thickness results for TG4 and TG6 nozzles at 15 mm nozzle height. Because of the hollow spray core center, the pressure gradient caused by droplet impingement (Equation 4.2) is unfavorable near the center (up to 3.5 mm for TG4, 15 mm nozzle height). So the film thickness decreases to provide the pressure gradient to keep the liquid flowing out. This is reflected in the figures. Superficially, it would appear that higher mass flow rate will make the film thicker. But with the increase of the mass flow rate, the nozzle inlet pressure and therefore the droplet velocity also increases. Higher droplet velocity causes higher pressure on the film (Equation 4.1), which makes the film thinner. Combining these two factors, as seen from Figures 4.11 and 4.12, the film thickness decreases slightly with the increase of liquid flow rate and nozzle inlet pressure.

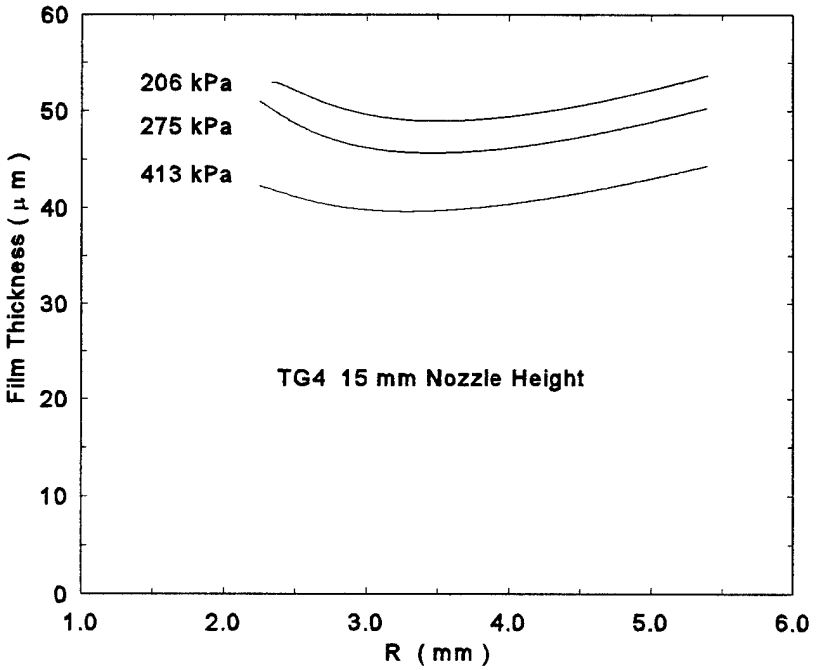

Figure 4.11 Film Thickness, Numerical Results for TG4 Nozzle

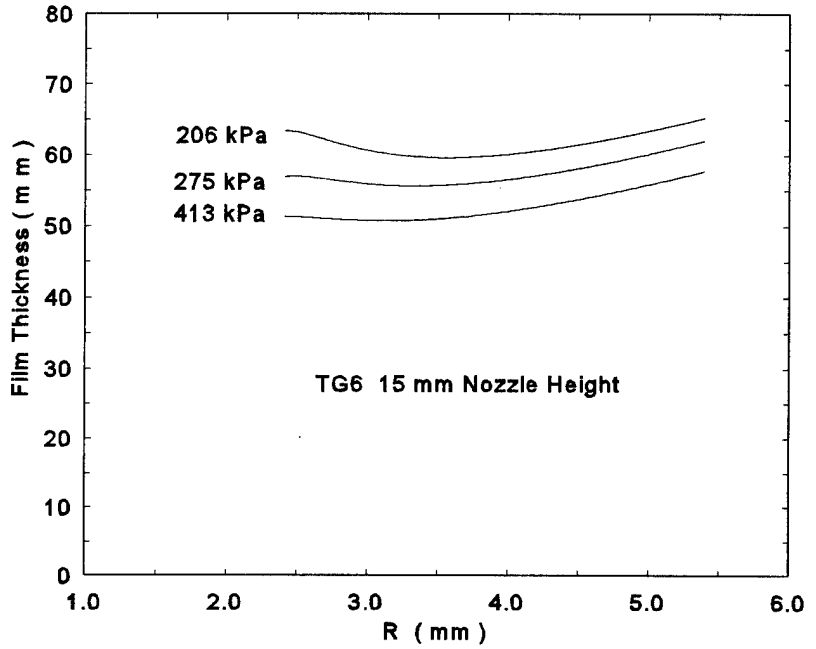

Figure 4.12 Film Thickness, Numerical Results, TG6 Nozzle

The effect of the nozzle orifice diameter on the film thickness is also directly related to the mean droplet velocity and the liquid flow rate, and the results show that the droplet velocity has a significant effect on the film thickness. Figures 4.13 and 4.14 illustrate the comparison of film thickness results of TG4 and TG6 at same nozzle inlet pressure (Figure 4.13) and same liquid flow rate (Figure 4.14). When the nozzle operating pressure is fixed, nozzles with a larger orifice (TG6) have lower droplet velocity and higher flow rate (Table 4.1). This results in a thicker film compared with that of the nozzle with a smaller orifice (Figure 4.13). For a fixed liquid flow rate, nozzles with a smaller orifice have higher droplet velocity and therefore thinner liquid film (Figure 4.14).

The effects of nozzle height are not as significant. The mean droplet velocity drops only about 5% for the distance from 10 mm to 15 mm. This is not enough to make a perceptible difference. Therefore, despite the change of the local liquid flow rate for different nozzle heights, the film thickness remains almost unchanged. Figure 4.15 shows the comparison of numerical results of TG4 at 10 and 15 mm nozzle height. We can also see this in the experimental results shown in Table 4.2. This proves that the droplet velocity is the dominant factor for the film thickness in the spray core.

Mass flow rate distribution can also significantly affect the film thickness. Figure 4.16 shows the comparisons of the film thickness results of TG6 when the two different mass flow rate distributions represented by Equations 4.9 and 4.10 are applied. The distribution of Equation 4.9 has a larger hollow area at the center and mass flow is more concentrated near the edge. This results in a thinner film near the edge as compared with that if Equation 4.10 is used.

The numerical results were compared against the experimental measurements. For this purpose, the numerical results obtained at R = 5 mm were used since the film thickness is measured at that radius during the experiments. For the flow rate profile like Equation 4.9, where the liquid flow is more concentrated near the edge, the numerical solution yields slightly thinner film compared with the experimental results. The numerical solution with the flow rate profile given by Equation 4.10 gives better results. Both profiles can give a prediction of the film thickness within ± 20%, but the results with Equation 4.10 have a better accuracy, about ± 10%. Considering the inevitable circumferential mal-distribution and its effect on the film thickness, this accuracy can be considered acceptable. Since there is only a slight change in the Sauter mean diameter of the droplets (from 120 μm to 132 μm) for the two nozzles and the pressure range used in the

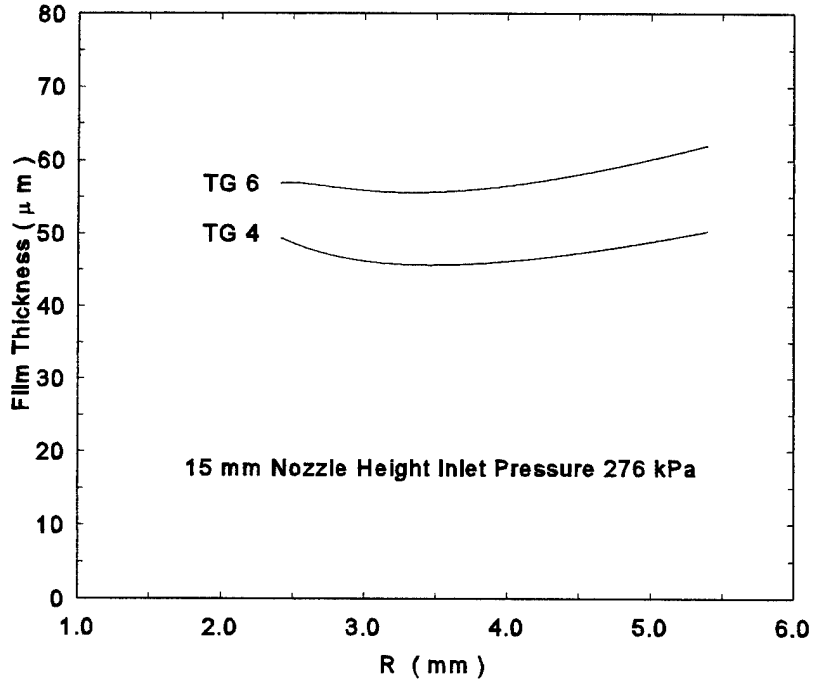

Figure 4.13 Film Thickness Comparison, Same Inlet Pressure

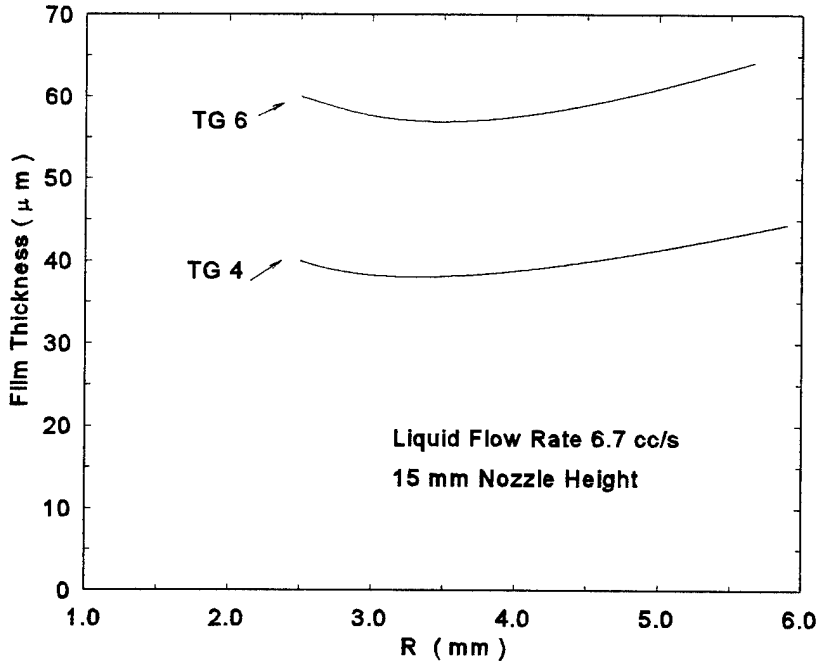

Figure 4.14 Film Thickness Comparison, Same Flow Rate

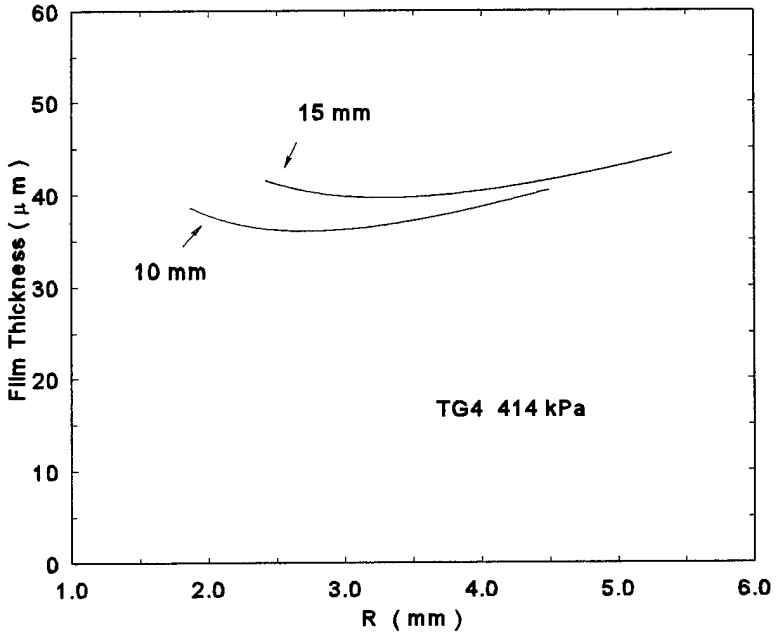

Figure 4.15 Effect of Nozzle Height

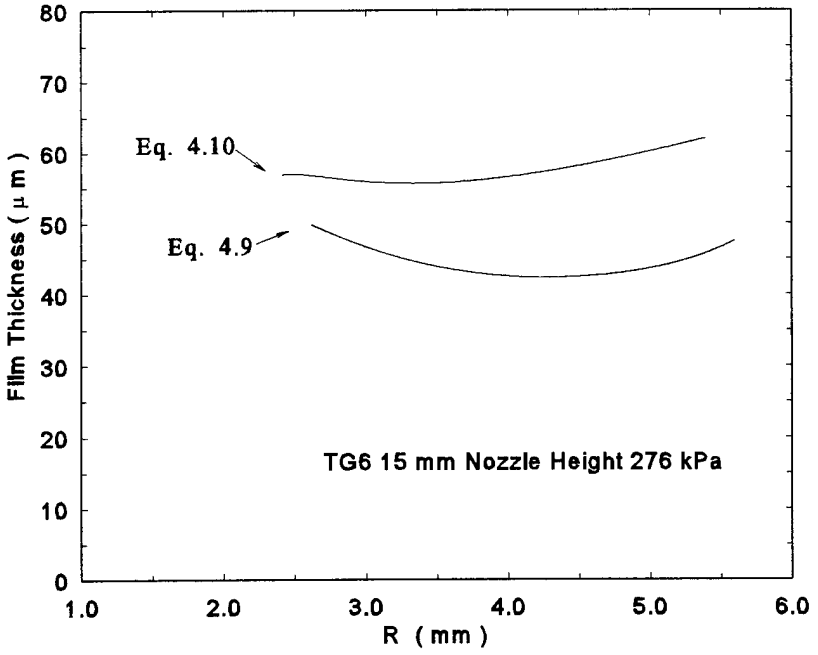

Figure 4.16 Effect of Mass Flux Profile

experiments, the effects of droplet diameter on the film thickness remains unclear in the present study.

4.5.2 Film Thickness for Air Atomizing Nozzle

Yang et al. [19,21,22,29] analyzed the film thickness produced by an air atomizing nozzle using a two-layer model. The top layer is the air flow of a round impinging jet, and the bottom layer is the liquid film. The driving force for the flow in the liquid film is the pressure gradient caused by the impinging air jet and the shear force at the film surface. Because of the small liquid flow rate (< 1.2 cc/s compared with > 4.9 cc/s for pressure atomizing nozzles discussed earlier) and the high pressure caused by impinging air jet, the effects of droplet impingement are neglected.

4.5.2.1 Air Stagnation Flow

The top (air flow) layer can be divided into three regions: the free jet region, the stagnation flow region and the wall jet region. In the free jet region, the jet exchanges momentum with the surrounding fluid and the boundary of the free jet widens. In the stagnation flow region, the vertical velocity component transforms into the accelerating horizontal velocity. The velocity components in this region outside the boundary layer are given by [30,22,29]:

$$u = arF'(\eta); \qquad w = -2az; \qquad \eta = z\sqrt{\frac{a}{\nu_a}} \tag{4.12}$$

The pressure profile in this region can be expressed as [11]:

$$p_a = p_0 - \frac{1}{2}\rho_a a^2(r^2 + F(z)) \tag{4.13}$$

Here "a" is an empirical constant. Schrader [30,31] determined "a" to be:

$$a = \left(\frac{V_{air}}{D}\right)\left(1.04 - 0.034\frac{H}{D}\right) \tag{4.14}$$

where H is the nozzle height from the surface, D is the orifice diameter and V_{air} is the air velocity at the nozzle exit.

The wall jet region, where all the vertical velocity components have converted to horizontal velocity, is not important for this case, because the area we are interested in (~12 mm diameter) is almost fully covered by the jet with a diameter of about 11 mm, 20 mm away from the orifice.

4.5.2.2 Flow of Liquid Film

The film flow on the surface is a viscous boundary layer problem with a free surface. As shown in the experimental results, the film produced by the air atomizing nozzle is very thin (< 80 μm) and the liquid flow rate in the film is very small (<1.2 cc/s). The maximum Reynolds number of the film is less than 37 (4.2 liters/cm^2 hr, average film velocity is used, at the edge of the spray core). As a typical low Reynolds number flow, the inertia forces can be neglected when compared to the viscous forces. So the boundary layer equation for the film flow can be written as:

$$0 = \frac{\partial p}{\partial r} + \mu_l \frac{\partial^2 u_l}{\partial z^2} \tag{4.15}$$

with the boundary conditions:

$$\begin{aligned} u_l &= 0 && at \quad z=0 \\ \tau_s &= \mu_l \frac{\partial u}{\partial z} && at \quad z=h(r) \end{aligned} \tag{4.16}$$

Here, τ_s is the surface shear force at the air-liquid interface:

$$\tau_s = \mu_a \frac{\partial u}{\partial z}\Big|_a = \mu_l \frac{\partial u}{\partial z}\Big|_l \tag{4.17}$$

Substituting Equation 4.12 into Equation 4.17:

$$\frac{\partial u}{\partial z}\Big|_l = 1.312 \sqrt{\frac{a^3 \mu_a \rho_a}{\mu_l^2}}\, r = Cr; \qquad F''(0) = 1.312, \quad [17] \tag{4.18}$$

Integrating Equation 4.15 twice and applying the boundary conditions (Equation 4.16 and 4.17), the liquid velocity can be obtained as [29]:

$$u_l = \frac{\rho_a}{\mu_l} r a^2 z \left(h - \frac{z}{2}\right) + Crz \tag{4.19}$$

If we assume a uniform liquid flux, $\dot{m}$, in the spray core, the continuity equation can be written as:

$$2\pi r \int_0^{h(r)} u_l dz = \pi r^2 \dot{m} \tag{4.20}$$

Substituting Equation 4.19 into Equation 4.20, we can get the following equation for the liquid film thickness [29]:

$$\dot{m} = \frac{2}{3} \frac{\rho_a}{\mu_l} a^2 h^3 + 1.312 \sqrt{\frac{a^3 \mu_a \rho_a}{\mu_l^2}} h^2 \tag{4.21}$$

It can be noted that h is not a function of r in the above equation.

4.5.2.3 Results and Discussion

The spray nozzle used in this experiment has a unique conical design (Figure 4.7) which results in a fast boundary expansion (from 0.7 mm to 10 mm within 20 mm distance) that cannot be achieved with ordinary jet nozzles. Since Equation 4.14 was obtained for ordinary jet nozzles, a nozzle with an orifice diameter of 10 mm is assumed instead of the actual diameter of 0.7 mm. At 20 mm from the orifice, this air atomizing nozzle will have about the same jet diameter as an ordinary jet nozzle with a 10-mm orifice. This assumption makes Equation 4.14 applicable in this case.

Average air velocity and liquid flux are used to calculate the film thickness. Table 4.5 lists the calculated results and their comparison with the measurements. The calculated results are close to the measurements and correctly reflects the increase of film thickness with liquid flow rate. The theoretical results also show that higher air pressure (higher air velocity) results in thinner liquid film.

Table 4.1 Film Thickness of Air Atomizing Nozzle
Nozzle Height 20 mm

Air Pressure	Liquid Volume Flow rate [liters/hr]	1.2	1.8	2.4	3.0	3.6	4.2
138 kPa (20 psi) V_m=35 m/s	Calculated Film Thickness (μm)	45	54	61	67	71	78
	Measured Film Thickness (μm)	50	60	65	75	78	80
207 kPa (30 psi) V_{max}=48 m/s	Calculated Film Thickness (μm)	36	43	48	54	58	62
	Measured Film Thickness (μm)	35	40	42	45	47	50
276 kPa (40psi) V_m=55 m/s	Calculated Film Thickness (μm)	33	39	44	49	55	56
	Measured Film Thickness (μm)	22	30	30	35	42	45

4.6 Uncertainty Analysis

The uncertainty in droplet velocity measurement depends on the PDPA system. The velocity distribution of the droplets for any location is always Gaussian with a standard deviation of 2-4 m/s and is reasonably repeatable. The overall uncertainty in the mean droplet velocity is less than 5 % for the velocity range measured. The liquid flow rate measured using the orifice meter and the pressure transducer is calibrated using a graduated cylinder and a stop watch. The uncertainty in the measured volume is ± 2 cc and the uncertainty in the time is ± 0.5 s. This results in an average uncertainty of ± 0.2 cc/s in the volumetric flow rate measurement. The uncertainty in the nozzle inlet pressure is about 2 % as read from a grade gauge.

Several steps are followed to measure the film thickness, as shown in Figure 4.5. The steps that determine the positions of point B and C and the step to set the initial point in the experiment are most important for the accuracy. The uncertainty in finding the positions of points B and C are about ± 5 μm and the error in finding the initial point is about ± 3 μm. This gives a maximum

uncertainty of ± 13 μm in the film thickness measurements. The film thickness measurements of air atomizing nozzle have the same uncertainty because an average is used for the position of the wavy film surface. The uncertainty related with this process is also about ± 5 μm.

5. EFFECTS OF OPERATING TEMPERATURE AND THERMAL MANAGEMENT TECHNIQUES ON MOSFET CHARACTERISTICS

Even though the power MOSFETs operate more efficiently at cryogenic temperatures, it was shown in a recent study that the break-even temperature from an energy saving point of view was close to 150 K [33]. This is because maintaining the circuit at a low temperature involves refrigeration penalties which have to be taken into account when evaluating the overall efficiency.

Despite the higher efficiency of cryogenic temperature electronics, the waste heat dissipation will remain a problem. The objective of this part of the study is to examine the potential challenges in thermal management of superconductor/semiconductor hybrid circuits. In the following sub-sections, the improvement in maximum drain current of some MOSFETs operating at a low temperature are compared against the operating temperature and the thermal management technique.

5.1 Maximum Drain Current of Power MOSFETs

The MOSFETs used in power conversion applications (e.g., generator supplying a radar load) can have very high power dissipations. At room temperature, IRFBG30, a 1000V MOSFET in a TO-218 package, is rated at 125 watts [34]. Since the effective heat transfer area of the package base is less than 1 cm^2, this MOSFET is capable of dissipating over 125 W/cm^2 without failure. The power rating (P_D) of the MOSFET is based on the thermal resistance of its packaging. In general, a 125 W rating means that 125 W can be conducted out by the packaging if the casing surface is maintained at 25°C and the maximum allowable junction temperature is 150°C. This translates in to a thermal resistance of 1 °C/W for the thermal packaging of the MOSFET mentioned previously. The thermal resistance between the junction and the case surface is made up of resistance due to silicon and the copper base in addition to the interfacial resistance between copper and silicon. The interfacial resistance is mainly due to a very thin layer of metallization and solder which connects the copper to silicon die. For cryogenic operation, there are two main advantages. The on-resistance ($R_{DS(on)}$) of the MOSFET decreases by an order of magnitude [35]. At the same time, the thermal conductivities of copper and silicon increase significantly [11]. In conjunction these factors enable a MOSFET to carry a much higher drain current at cryogenic temperatures as compared to its

normal rating.

Under normal circumstances, the maximum allowable continuous drain current, $I_{D(max)}$, in a MOSFET is given by:

$$I_{D(\max)} = \sqrt{\frac{P_D}{R_{DS(on)(at\ T_{j\max})}}} \tag{5.1}$$

Here, $T_j(max)$ refers to the maximum allowable junction temperature which is generally 150 °C. Usually, the manufacturer rates the $I_{D(max)}$ by including the thermal resistance of the insulation which has to be put between the case and the heat sink. The value of this resistance is typically assumed to be 0.5 °C/W. Then, the heat sink temperature is assumed to be 25 °C to calculate the P_D and the resulting $I_{D(max)}$ rating. Thus, the rated P_D (125 W in the previous case) is only applicable if the case surface is somehow maintained at 25 °C.

Let us consider the 1000V MOSFET, IRFPG50 (International Rectifier classification) in a TO-247AC packaging with power rating of 190 W. The detailed schematic diagram of this MOSFET is shown in Figure 5.1. The thermal resistance of the packaging is 0.66 °C/W [36]. At normal operating temperatures, the main contribution to this resistance is due to the silicon wafer. This MOSFET is rated at 6.1 A (maximum continuous drain current) for room temperature operation. As mentioned earlier, this rating of $I_{D(max)}$ accounts for the thermal resistance between the case and the heat sink in addition to the junction-case thermal resistance; i.e., the total thermal resistance increases to 1.16 °C/W. This decreases the power rating used for calculating $I_{D(max)}$ from 190 W to 108 W. The $R_{DS(on)}$ for this MOSFET is 1.6 ohm at a junction temperature of 303 K, and 0.11 ohm at a junction temperature of around 78 K [35]. Assuming that the on-resistance varies linearly with junction temperature, the on-resistance dependence on junction temperature is given by:

$$R_{DS(on)(T_j)} = 0.11 + 6.6 \times 10^{-3}(T_j - 78) \tag{5.2}$$

Secondly, the thermal conductivity of pure silicon increases from 148 W/m.K at 300 K to 1340

W/m.K at 80 K, and that of copper increases from 398 W/m.K at 300 K to 580 W/m.K at 80 K [11]. The exact thermal conductivity of n-type silicon used in this MOSFET is uncertain because it varies significantly with the level of doping and direction with respect to the crystal axis [11]. If we make a conservative estimate that the silicon die has a thermal conductivity of 619 W/m.K, which is the lowest measured conductivity of pure n-type silicon crystal at 80 K, then the thermal resistance due to the silicon is less than 0.02 °C/W at this temperature.

In order to determine the thermal resistance due to the copper base, a detailed numerical analysis was carried out using the ANSYS finite element analysis program. The thermal resistance was calculated by keeping the base at a constant temperature of 78 K and applying a known constant heat flux at the die location. The results of the analysis indicate that the thermal resistance of the

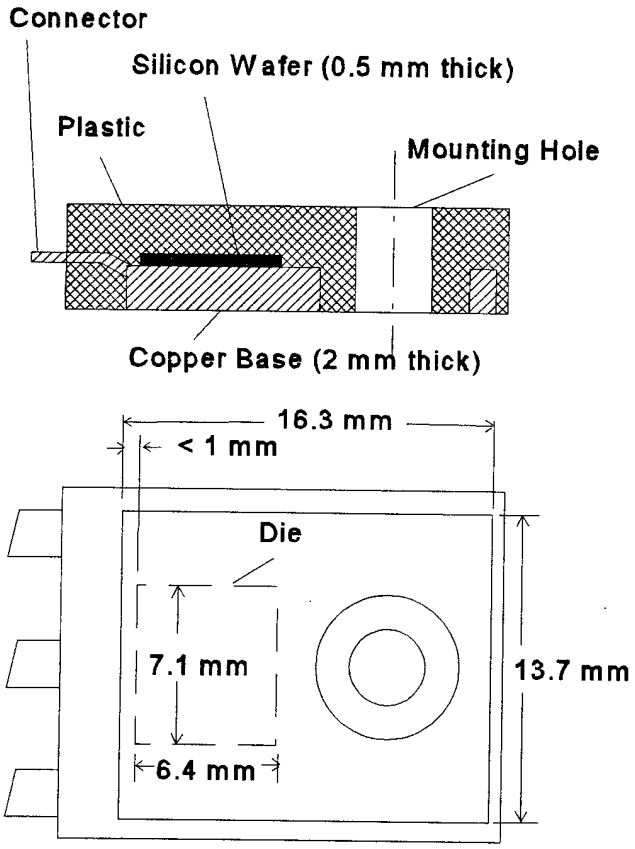

Figure 5.1 Physical Details of the IRFPG50 MOSFET

copper base is 0.05 °C/W; i.e., for 100 W power dissipation, the average temperature of the copper in contact with the die is about 5 K higher than the case surface.

The thermal resistance due to the solder and the metallization between the copper and the silicon is much lower due to the very small thickness of the two (estimated to be less than 0.05 mm). Using a conservative value for this resistance, the overall thermal resistance is estimated as 0.09 °C/W at 80 K.

The variations in thermal conductivities between 80 K and 300 K are non-linear and quite complex for both copper and silicon. Further, the exact thermal characteristics of the silicon used in the die are not known. Hence, it is difficult to know the exact thermal resistance at temperatures between 80 K and the normal operating temperature. Making a simplifying assumption that the overall junction-case thermal resistance varies linearly between 80 K and 360 K (the mean temperature of the chip when the junction is at 150 °C and the case is at 25 C), the thermal resistance variation can be approximated by Equation 5.3. Here, T refers to the mean temperature of the chip, i.e., the average of junction temperature and the base temperature.

$$R_{th,j-c} = 0.09 + 2.1 \times 10^{-3}(T - 80) \tag{5.3}$$

Using Equations 5.3, the maximum power that can be dissipated by the MOSFET is approximated by:

$$P_D = \frac{T_j - T_c}{0.09 + 2.1 \times 10^{-3}\left(\frac{T_j + T_c}{2} - 80\right)} \tag{5.4}$$

where all temperatures are in Kelvins. Considering Equations 5.1 to 5.4, and assuming T_c is maintained at 78 K (for liquid nitrogen temperature operation), we can obtain the chart shown in Figure 5.2.

From Figure 5.2, it can be seen that the maximum drain current can be more than quadrupled by operating at liquid nitrogen temperature. The maximum drain current of 29 A occurs at a junction

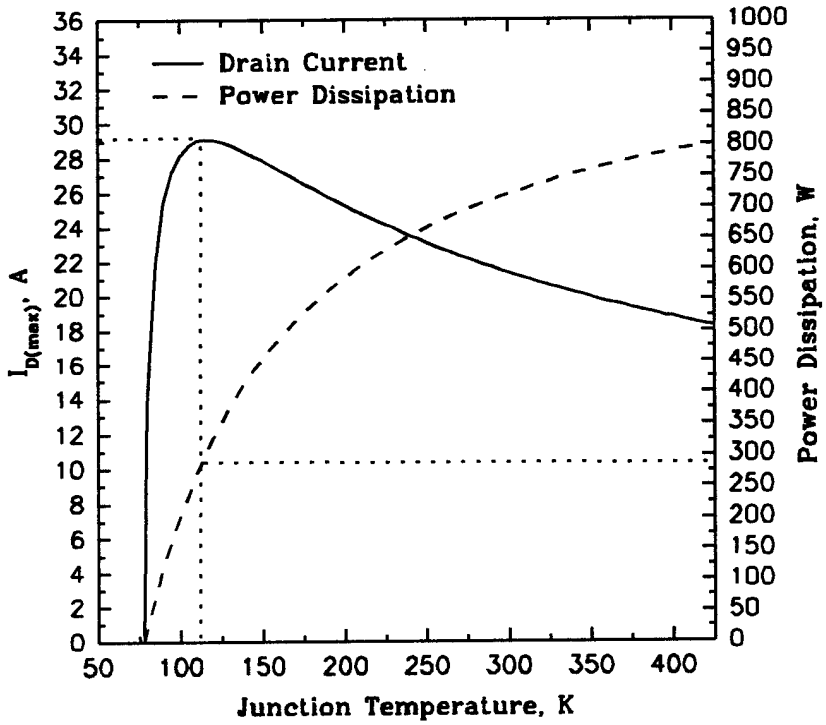

Figure 5.2 Power Dissipation and Drain Current Characteristics of IRFPG50 at Liquid Nitrogen Temperature

temperature of 112 K. At this current, the power dissipation is about 280 W. From the dimensions of the TO-247AC, the copper base area is about 2 cm^2 (discounting the area occupied by plastic). However, the die area is only 0.45 cm^2 and the die is placed extremely close to the edge of the copper base. Considering the heat spreading ability of the copper base, the effective heat transfer area on the base is not more than 1.2 cm^2. Referring to Figure 5.1, this is the area bounded by a 13.7 mm x 9 mm rectangle extending from the left edge of the mounting hole to the edge of the copper base. This was also confirmed by the finite element analysis carried out to determine the thermal resistance of the copper base. Calculating the heat flux based on this area gives a heat flux of about 2300 kW/m^2 at the maximum drain current. At a marginally lower current of 25 A, the heat flux would reduce to 1015 kW/m^2; and at a current of 22 A, the heat flux would be 625 kW/m^2.

The heat flux and maximum current estimates are on the conservative side due to the assumptions mentioned earlier. Further, if different packaging (more compact) is used, much higher heat fluxes are possible.

The drain current curve in Figure 5.2 shows a maximum, i.e., there is a junction temperature above which the drain current decreases. The location of the peak prior to the junction temperature of 423 K (maximum allowable junction temperature) depends on the relative slopes of the thermal resistance and the on-resistance curves. In order to illustrate this, let us consider MOSFET MTM5N100 (1000V, 5A, 3 ohm, 150W) which comes in a TO-218AC packaging which is almost identical to TO-247AC package [37]. According to Mueller [37], the on-resistance of this MOSFET drops to 0.17 ohm at liquid nitrogen temperature. Carrying out similar calculations for this MOSFET, Figure 5.3 is obtained.

From Figure 5.3, it can be seen that the drain current has a maximum at 120 K. At this

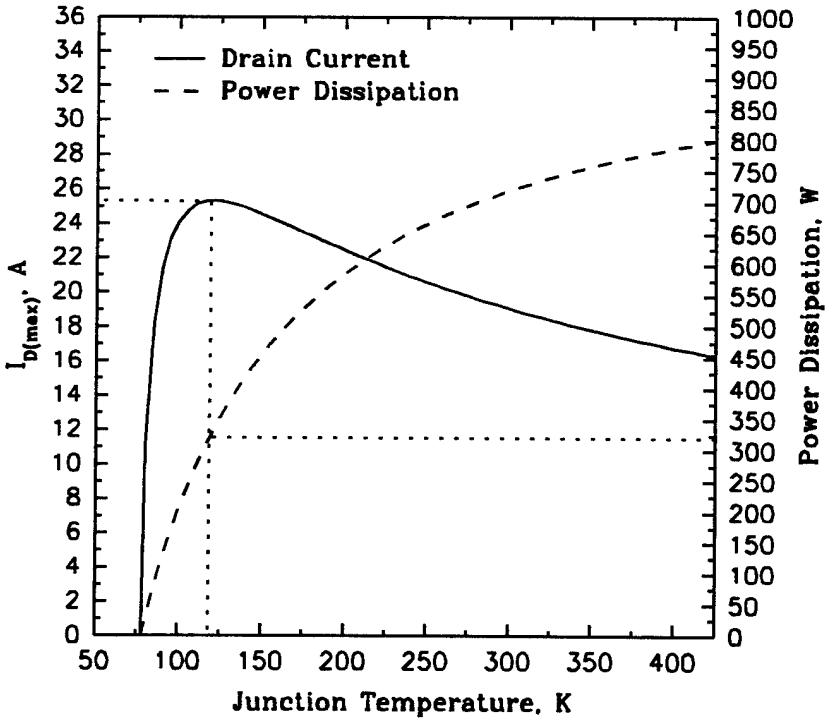

Figure 5.3 Power Dissipation and Drain Current Characteristics of MTM5N100 at Liquid Nitrogen Temperature

junction temperature, the drain current reaches a maximum value of 25.3 A (with power dissipation of 325 W). For this MOSFET, the power dissipation at 22 A is about 145 W. Since the effective heat transfer area of this packaging is also about 1.2 cm^2, heat fluxes over 2500 kW/m^2 are possible with this MOSFET.

From this discussion, it is clear that heat fluxes on the order of 1000 kW/m^2 are possible if high drain currents are used. Taking the calculated heat fluxes into consideration, the options available for the thermal management are:

1. Immersion cooling with low device density packaging and employing heat spreaders (or operating the device at a fraction of the maximum drain current).
2. High heat flux cooling methods, e.g., flow boiling and spray cooling.

As mentioned in Section 3, the first option cannot be expected to handle device heat dissipation above 300 kW/m^2 even with the use of a heat sink. This is because the pool boiling critical heat flux for the prospective cryogens in the 78-150 K range is on the order of 150 kW/m^2. In cases where higher heat dissipation needs to be handled, the second option of using a high heat flux cooling technique would be much more preferable. The high heat flux cooling techniques, which include spray cooling, submerged jet impingement cooling, and flow boiling, are expected to be able to remove over 1500 kW/m^2 at cryogenic temperatures.

In the previous analysis, it was assumed that the case surface was at 78 K. This was a simplifying assumption which is not entirely valid because the fluid (LN_2) itself is at 77.3 K. The external thermal resistance, i.e., that between the case surface and the fluid, was not accounted for in the previous calculations. This external thermal resistance depends on the cooling technique. The following section compares two cooling techniques and obtains the resulting drain current capacities of the IRFPG50 MOSFET discussed previously.

5.2 Effect of Cooling Technique on Drain Current Capacity

The easiest cooling technique which can be applied in cryogenic cooling is immersion cooling. According to the correlation provided by Zuber [15], for liquid nitrogen, the cooling capacity (maximum heat flux) of this technique is limited to about 164 kW/m^2. Higher heat fluxes may be removed by employing heat spreaders on the chip. However, the heat spreader also adds to

the thermal resistance; therefore, the addition of a heat spreader may not be as beneficial as it appears on the surface. Various kinds of heat spreaders have been developed for immersion cooling. Their characteristics differ greatly, and therefore, no calculations using heat spreaders were carried out. The following analysis only considers the bare chip cooled by the liquid directly.

For pool boiling (immersion cooling) with liquid nitrogen, the heat flux dependence on the temperature of the surface is given by Kutateladze's correlation [38] which can be expressed as:

$$q'' = C(T_{surface} - T_{sat})^{2.5} \tag{5.5}$$

where C is 345 $W/m^2.K^{2.5}$ for liquid nitrogen. Thus, we can calculate the surface temperatures for heat fluxes less than 164 kW/m^2. Note that this is the heat flux; in order to evaluate the average junction temperature using the thermal resistance we need the total power dissipation. This has to be calculated by multiplying the effective heat transfer area of the chip package with the heat flux. As previously mentioned, the effective heat transfer area of the IRFPG50 MOSFET is about 1.2 cm^2.

Using the surface temperatures (which are the case temperatures) and the total heat dissipation, the junction temperature can be evaluated from Equation 5.4. Then, the on-resistance can be obtained from the Equation 5.2. Finally, using the power dissipation and the on-resistance, the drain current can be calculated. This way, the junction temperature vs. drain current curves can be obtained for immersion cooling.

The immersion cooling performance is compared against spray cooling with liquid nitrogen. As shown in a previous report [2], spray cooling with liquid nitrogen can remove heat fluxes over 1600 kW/m^2. The performances of various spray nozzles are given in References 2 and 3. Here, we use the performance characteristics of FL#13 nozzle at 828 kPa with resulting flow rate of 1.0×10^5 $kg/hr.m^2$. The heat flux varies almost linearly with the superheat (difference between the surface temperature and the saturation temperature of the liquid). For these parameters, the heat flux is given by Equation 5.6. Using the same technique as before, the junction temperature vs. drain current

$$q'' = 9.14 \times 10^4 (T_{surface} - T_{sat}) \tag{5.6}$$

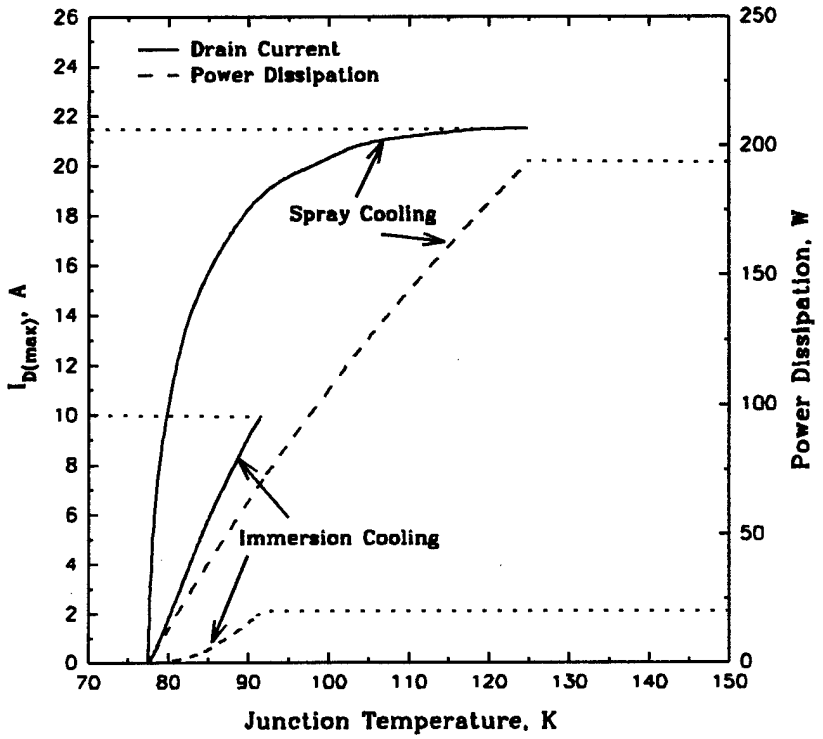

Figure 5.4 Comparison of Immersion Cooling and Spray Cooling with Liquid Nitrogen

curve for spray cooling can be obtained. The resulting temperature-current-power characteristics of the IRFPG50 MOSFET cooled using the two cooling techniques are shown in Figures 5.4.

As seen from Figure 5.4, the high heat flux technique (spray cooling) permits a higher drain current at any junction temperature. This is due to its lower external (case-fluid) thermal resistance. Both cooling techniques result in an improvement over room temperature operation. It can be seen that the maximum drain current with spray cooling is less than that in Figure 5.2 (for the case temperature at 78 K). This is due to the presence of the external thermal resistance. It should be noted that these calculations were intended to illustrate the difference due to the two cooling techniques. The absolute values of the drain current and power dissipation may be in error due to the estimate of the effective heat transfer area of the chip and the neglecting of the heat loss through the plastic part of the package. However, the relative differences in the drain current due to the two cooling techniques should be accurate.

5.3 Operating Electronics at 150 K

As mentioned earlier, a thermodynamic analysis carried out by Donovan et al. [33] showed that the break-even temperature (for energy savings) for the operation of cryo-electronics was 150 K. Let us examine if operating at 150 K results in any advantage over room temperature operation. Considering IRFPG50 and carrying out the first analysis, only this time keeping the case temperature at 150 K instead of 78 K, we can obtain the curves shown in Figure 5.5.

As seen from Figure 5.5, the drain current can still be improved significantly beyond the room temperature limit (6.1 A). However, the heat dissipation is significantly higher as compared to 78 K operation. For example, at 10 A, the heat dissipation at 78 K was less than 20 W, but, at 150 K, the heat dissipation is about 70 W. This is due to the higher on-resistance at these junction temperatures. Thus, drain current enhancement at 150 K can only be obtained by dissipating higher heat fluxes as compared to 78 K operation. Even for a drain current of 6.1 A (rated current at room

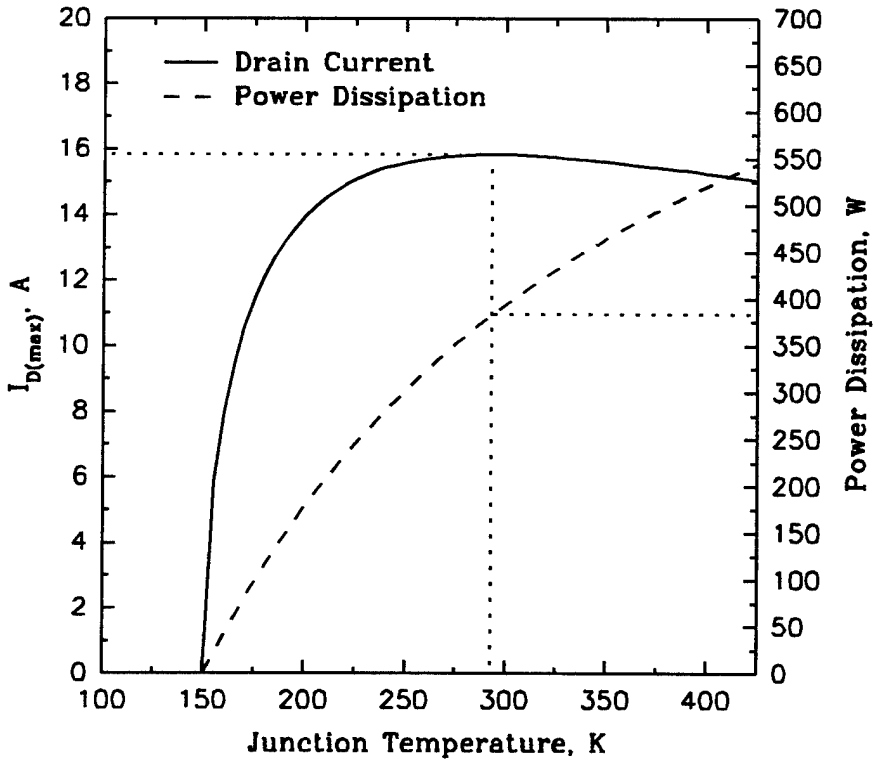

Figure 5.5 Power Dissipation and Drain Current Characteristics of IRFPG50 at 150 K

temperature), heat dissipation is close to 25 W (or 200 kW/m^2 for the 1.2 cm^2 heat transfer surface). This value will increase further if the external thermal resistance is considered. This may be higher than the immersion cooling critical heat flux limit for the cryogen used for this temperature range. Therefore, the use of a high heat flux cooling technique is even more appropriate for 150 K operation.

Since pool boiling and spray cooling characteristics of the cryogens to be used for 150 K operation are uncertain, no comparison plot similar to Figure 5.4 was obtained. However, there is no reason to expect any significant difference in trends for this case.

6. CONCLUSIONS AND RECOMMENDATIONS FOR FUTURE WORK

A method using the point gauge was developed to measure the water film thickness in the spray core for pressure and air atomizing nozzles. Analytical models, which agree quite well with the measured results, were also developed. These models can be easily extended to predict the film thicknesses produced by other liquids.

For the pressure atomizing nozzles, the experimental results show that the film thickness is around 50 μm for the two nozzles tested. The effect of the nozzle height on the film thickness is insignificant for the two heights (10 mm and 15 mm) tested.

For the air atomizing nozzle, measurements showed that the film thickness increases with the liquid flux. At a fixed liquid flux, the film thickness decreases with increase in air pressure (or air velocity). The film thickness produced by the air atomizing nozzle used in the experiment is comparable with that of pressure atomizing nozzles even through the liquid flow rate is very different. The film thickness was less than 100 μm for all the tested situations.

An integral method that incorporates the effect of mass flow rate distribution is used in the numerical analysis for the pressure atomizing nozzle. The results agreed well with the experiment and show the following properties of the film in the spray core: the mean droplet velocity and the radial mass flow rate distribution are the main factors that affect the liquid film thickness in the spray core of pressure atomizing nozzles; for each nozzle, the film thickness decreases with the increase of the nozzle inlet pressure and liquid flow rate; nozzles with a smaller orifice diameter have thinner liquid films at the same nozzle operating pressure (or the same liquid flow rate); the radial and circumferential mass flow rate distribution affects the film thickness and also the shape of the film surface. The numerical method incorporating the two correlations of mass flux distribution provided in this study can predict the water film thickness with an accuracy of ± 20%. Equation 4.10 achieved better accuracy for the two nozzles tested.

An analytical method incorporating a two-layer model and the surface shear stress is used for the film thickness analysis of the air atomizing nozzle. For the upper air jet, a semi-empirical correlation is used for the pressure profile. Because the lower layer, the liquid film, has a low Reynolds number, the inertia terms are dropped in the boundary layer equation. The average liquid

flux and the average air velocity from the measurements are used in the final equation. The analytical results agree well with the film thickness measurements. The analytical results also show that the film thickness is independent of the radius, increases with increase in liquid flux, and decreases with increase in air velocity.

As mentioned earlier, both models can be used for other liquids. With this study, an important gap in spray cooling knowledge has been filled. Detailed modeling of the spray cooling process will now be easier to accomplish.

In the other part of this study, a numerical analysis was carried out for power MOSFETs IRFPG50 and MTM5N100 to determine the heat dissipation and drain current characteristics for 78 K and 150 K operation. Further comparisons were made between immersion cooling and spray cooling with liquid nitrogen. It was seen that if an ideal cooling technique is available, i.e., one that can maintain the case temperature almost equal to the fluid temperature, the drain current can be more than quadrupled for 78 K operation. However, higher drain currents will require the use of a high heat flux removal technique like spray cooling.

In comparing different cooling techniques using liquid nitrogen, it was seen that the maximum drain current that can be sustained by spray cooling was more than twice the current that can be sustained by immersion cooling. At similar junction temperatures, spray cooling enables a significantly higher drain current as compared to immersion cooling. For the same drain current, the power dissipated under spray cooled condition is lesser because of the lower on-resistance (due to the lower junction temperature).

For 150 K operation, the heat dissipation increases as compared to 78 K operation. For this temperature, a high heat flux technique needs to be used to obtain any improvement in drain current over room temperature operation.

This report, which is the fifth and the final report for contract F33615-91-C-2152, addressed the film thickness estimation aspect of spray cooling and cryogenic operation of power MOSFETs. The overall study has advanced the knowledge of spray cooling, pool boiling and free expansion, particularly in reference to using cryogens. Semi-empirical correlations, which are suitable for thermal design, have been derived for these processes. In order to gain a detailed understanding of the cooling processes, future studies should focus on high-heat-flux cooling (spray, flow and jet

impingement cooling) of densely populated heat sources in complicated geometries. The effect of heat source surface characteristics (viz., surface material, roughness, protrusion with respect to the surrounding surface) on the heat transfer characteristics should also be investigated. In addition to these fundamental studies, investigations should be carried out to determine the possible size/weight reductions in the overall system when using cryo-electronics. This would include an investigation into, and selection of, appropriate cryocoolers.

7. REFERENCES

1 Chow, L. C., Sehmbey, M. S., Pais, M. R., Lu, W. F., and Hahn, O. J. "Fundamental Studies in Hydrogen Blow-down and Cryogenic Cooling," Wright Laboratory Technical Report No. WL-TR-93-2081, August 1992.

2 Chow, L. C., Sehmbey, M. S., Lu, W. F., Pais, M. R., and Hahn, O. J. "Fundamental Studies in Blow-down and Cryogenic Cooling," Wright Laboratory Interim Report No. WL-TR-93-2128, September 1993.

3 Chow, L. C., Sehmbey, M. S., Hahn, O. J., and Chui, C. J., "Fundamental Studies in Cryogenic Cooling of Power Electronics," Wright Laboratory Interim Report No. WL-TR-94-2100, September 1994.

4 Chow, L. C., Sehmbey, M. S., Hahn, O. J., and Lu, W., "Fundamental Studies in Cryogenic Cooling of Power Electronics," Wright Laboratory Interim Report No. WL-TR-95-2116, September 1995.

5 Nisenhoff, M., "Superconducting electronics: current status and future prospects," *Cryogenics*, Vol. 28, No. 1, pp. 47-56, 1988.

6 Van Duzer, T., "Superconductor-semiconductor hybrid devices, circuits and systems," *Cryogenics*, Vol. 28, No. 8, pp. 527-531, 1988.

7 Tucker, J. R., "Quantum limited detection in tunnel junction mixers," *IEEE Journal of Quantum Electronics*, Vol. QE-15, pp. 1234-1258, 1979.

8 McGrath, W. R., Raisanen, A. V., Richards, P. L., Harris, R. E., and Lloyd, F. L.,

"Accurate noise measurements of superconducting quasiparticle array mixers," *IEEE Trans. on Magnetics*, Vol. MAG-21, pp. 212-221, 1985.

9 Fox R. M., and Jaeger R. C., "MOSFET behavior and circuit considerations for analog applications at 77 K," *IEEE Trans. on Electron Devices,* Special Issue on Low Temperature Semiconductor Electronics, Vol. ED-34, No. 1, pp. 114-123, 1987.

10 Mueller, O., "Cryogenic power conversion: combining HT superconductors and semiconductors," AIP Conference proceedings 251, pp. 746-759, 1991.

11 Touloukian, Y. S., Powell, R. W., Ho, C. Y. and Clemens, P. G., *Thermophysical Properties of Matter The TPRC Data Series*, Vol. 1 & 2, IFI/Plenum, NY, 1970.

12 O'Conner, L., "High -Temperature Superconducting Motors," *Mechanical Engineering*, Vol. 116, No. 4, p. 32, 1994.

13 O'Conner, L., "Building Natural Gas Locomotives," *Mechanical Engineering*, Vol. 116, No. 4, pp. 82-84, 1994.

14 Lavine, A. S., and Bai, C., "An analysis of heat transfer in Josephson junction devices," *J. of Heat Transfer*, Vol. 113, pp. 535-543, 1991.

15 Zuber, N., "On the Stability of Boiling Heat Transfer," *J of Heat Transfer*, Vol. 80, pp. 711-720, 1958.

16 Sehmbey, M. S., Chow, L. C., Pais, M. R. and Mahefkey, E. T., "High heat flux spray cooling," *Heat Transfer in High Heat Flux Systems*, HTD-Vol. 301, pp. 39 - 46, ASME 1994.

17 Pais, M. R., Chow, L. C. and Mahefkey, E. T., "Surface roughness and its effects on heat transfer mechanism in spray cooling," *J. of Heat Transfer*, Vol. 114, pp. 211-219, 1992.

18 Tilton, D. E., "Spray cooling," Ph.D. dissertation, University of Kentucky, Lexington, KY, 1989.

19 Yang, J. D., "Spray cooling with an air atomizing nozzle," Ph.D. dissertation, University of Kentucky, Lexington, KY, 1993.

20 Gu, C. B., Su, G. S., Chow, L. C. and Pais, M. R., "Comparison of Spray and Jet Impingement Cooling", 29th ASME/AIchE National Heat Transfer Conf., Atlanta, August 1993, Paper 93-HT-20.

21 Yang, J. D., Chow, L. C. and Pais, M. R., "Liquid film thickness and topography determination using Fresnel diffraction and holography," *Experimental Heat Transfer*, Vol. 5, pp. 239-252, 1992.

22 Yang, J. D., Chow, L. C. and Pais, M. R., "An analytical model to determine the liquid film thickness produced by gas atomized sprays," 29th ASME/AIChE National Heat Transfer Conf., ASME Paper No. 93-HT-30, Atlanta, GA., 1993.

23 Siwon, B., "Experimental investigation of the liquid film by a gas-liquid spray jet impinging onto a flat surface", *Int. Comm. Heat Mass Transfer*, Vol. 20, pp. 665-674, 1993.

24 Azuma, T. and Hoshino, T. "The radial flow of a thin liquid film," *Bulletin of JSME*, Vol. 27, No. 234, pp. 2747-2754, 1984.

25 Fickett, A. P. and Kalhammer, F. R., "Water electrolysis," *Hydrogen: its technology and implications*, Vol. 1, CRC Press Inc., pp. 3 - 44, 1977.

26 Schlichting, H., *Boundary Layer Theory*, 7th Edition, McGraw-Hill Book Company, pp. 449-488, 1979.

27 Lefebvre, A. H., *Atomization and sprays*, Hemisphere Publishing Corporation, pp.298, 1989.

28 Ortman, J. and Lefebvre, A. H., "Fuel distribution from pressure-swirl atomizers," *AIAA J. Propul. Power,* Vol. 1, No. 1, pp. 11 - 15, 1985.

29 Yang, J. D., Chow, L. C., and Pais, M. R., "An analytical method to determine the liquid film thickness produced by gas atomized sprays", Accepted by ASME *Journal of Heat Transfer*, 1995.

30 Martin, H.,"Heat and mass transfer between impinging gas jets and solid surfaces," *Advances in Heat Transfer*, Vol. 13, pp 1-60, 1977.

31 Schrader, H., *VDI-Forschungsh*, 484, 1961.

32 White, F. M., *Viscous Fluid Flow*, McGraw-Hill Publishing Company, pp 172-180, 1974.

33 Donovan, B. D., Mahefkey, T., and Ramalingam, M. L., "Effects of Refrigeration in a Transportable Cryogenic Aerospace Application," IECEC Paper No. AP-34, ASME, 1995.

34 International Rectifier, "IRFBG30 Data Sheet", International Rectifier Product

Information Center, El Segundo, CA, 1996.

35 Mueller, O. M, and Herd, K. G., "Ultra-High Efficiency Power Conversion Using Cryogenic MOSFETs and HT-Superconductors," Proceedings of The 1993 IEEE 24th Annual Power Electronics Specialist Conference, pp. 772-778, 1993.

36 International Rectifier, "IRFPG50 Data Sheet", International Rectifier Product Information Center, El Segundo, CA, 1996.

37 Mueller, O. M., "On-Resistance, thermal Resistance and Reverse Recovery Time of Power MOSFETs at 77K," *Cryogenics*, Vol. 29, No. 10, pp. 1006-1014, 1989.

38 Rohsenow, W. M., "Boiling," *Handbook of Heat Transfer Fundamentals*, Edited by W. M. Rohsenow, J. P. Hartnett and E. N. Ganic, 2nd ed., McGraw-Hill, New York, Chap. 12, 1985.